Title

Rare deglacial-aged corals point to weaker El Niño in a colder world

Authors

R. A. Domeyko[1]* (rdomeyko@utexas.edu), J. W. Partin[1] (jpartin@austin.utexas.edu), Y. M. Okumura[1] (yukoo@ig.utexas.edu), K. Thirumalai[2] (kaustubh@arizona.edu), P. N. DiNezio[3] (Pedro.DiNezio@colorado.edu), A. E. Lawman[4] (alawman@coloradocollege.edu), F. W. Taylor[1] (fwileytaylor56@gmail.com), D. Liu[5] (dliu@ig.utexas.edu), L. Vetter[2] (lvetter@arizona.edu), C. R. Maupin[6] (crmaupinatx@gmail.edu), E. Garaebiti[7] (gesline@vanuatu.gov.vu), A. Kalo[7] (abelkalona@gmail.com), K. K. Kotra[8] (krishna.kotra@usp.ac.fj), L. A. Zuraw[9] (zurawl@citadel.edu), H.-M. Hu[10] (hsunming.hu@gmail.com), M. Inoue[11] (inouem@okayama-u.ac.jp), R. L. Edwards[12] (edwar001@umn.edu), C.-C. Shen[13] (river@ntu.edu.tw)

Affiliations

[1]Institute for Geophysics, The University of Texas at Austin, Austin, TX, USA
[2]Department of Geosciences, University of Arizona, Tucson, AZ, USA
[3]Department of Atmospheric and Oceanic Sciences, University of Colorado Boulder, Boulder, CO, USA
[4]Environmental Studies and Science Program, Colorado College, Colorado Springs, CO, USA
[5]Department of Geological Sciences, Jackson School of Geosciences, The University of Texas at Austin, Austin, TX, USA
[6]Department of Geography, Texas A&M University, College Station, TX, USA
[7]Vanuatu Meteorology and Geohazards Department, Port Vila, Vanuatu
[8]School of Agriculture, Geography, Environment, Ocean and Natural Sciences, The University of the South Pacific, Emalus Campus, Port Vila, Vanuatu
[9]Department of Chemistry, The Citadel, Charleston, SC, USA
[10]State Key Laboratory of Loess and Quaternary Geology, Institute of Earth Environment, Chinese Academy of Sciences, Xi'an 710061, China
[11]Department of Earth Sciences, Okayama University, Okayama, Japan
[12]Department of Earth and Environmental Science, University of Minnesota, Minneapolis, MN, USA
[13]High-precision Mass Spectrometry and Environment Change Laboratory, National Taiwan University, Taipei, Taiwan, ROC

*Corresponding author. Email: rdomeyko@utexas.edu

This manuscript is a non-peer reviewed preprint submitted to EarthArXiv and has been submitted for publication to Nature Communications.

Abstract

Extreme El Niño events, the warm phase of the El Niño–Southern Oscillation (ENSO), have increased in frequency since the late 20th century[1,2], intensifying concerns about ENSO's response to a changing climate and its far-reaching impacts on global weather. Yet climate-model projections of future ENSO behaviour remain divergent, and simulations under past glacial boundary conditions likewise lack consensus[3-5]. Past climate simulations are distinctive in that they can be directly evaluated against subannually-resolved palaeoclimate archives; however, such archives remain scarce beyond the Holocene. Here we combine the first monthly-resolved, multidecadal fossil coral oxygen-isotope records spanning the last deglaciation with new climate-model experiments to evaluate ENSO amplitude and extreme-event frequency under colder climates. The new coral data from Vanuatu – where a significant portion of interannual changes are driven by ENSO – reveal a reduction in interannual variance and extreme-event frequency ~12–15 thousand years ago relative to the late Holocene. The climate simulations reveal systematic increases in interannual variance and extreme-event frequency from the cold deglacial to the warm Holocene, with further intensification under anthropogenic warming. The concordance of natural archives with climate-model simulations demonstrates a robust climate-state dependence of ENSO and strengthens confidence in projections of more frequent extreme El Niño events in a warming future.

Main text

Introduction

The El Niño–Southern Oscillation (ENSO) is a dominant driver of year-to-year climate variability (Fig. 1a), causing major disruptions in global climate leading to regional extremes such as drought, flooding, marine heatwaves, and ecosystem reorganizations[1,2,6]**.** Yet major uncertainties remain regarding how ENSO responds to external forcing, in part because the observational record spans only ~150 years and is spatially limited, particularly in the tropical Pacific[7]. Uncertainties in pre-satellite sea-surface temperature (SST) measurements, as reflected in the increasing spread of ENSO amplitude estimates across observational products prior to the 1970s (Fig. 1f), limit our ability to place recent ENSO changes into a longer-term perspective. Likewise, climate models have improved in reproducing observed ENSO characteristics, but they project widely divergent ENSO responses to future CO_2 forcing, from substantial strengthening to weakening to no detectable change at all[3-5,8-11]. Models also disagree on past ENSO changes, with the Paleoclimate Modelling Intercomparison Project simulations showing similarly large inter-model spread across the deglaciation and Holocene[3,12]. These limitations underscore the need to constrain ENSO behaviour across a wider range of background climate states and evaluate model simulations against palaeoclimate records.

Recent palaeo-ENSO studies have begun to leverage an expanding range of high-resolution proxies and targeted climate simulations to evaluate how ENSO responds to large-scale climate forcing across the Holocene and deglaciation. Palaeoclimate reconstructions have provided important insights into changes in ENSO amplitude, event duration, and extreme-event frequency across diverse climate states[13-16], whereas modelling work has also highlighted ENSO's sensitivity to background climate conditions[17,18]. Despite this progress, data–model comparisons remain challenging because proxy archives differ in resolution, seasonality, and sensitivity to ENSO processes, and most palaeoclimate simulations are of insufficient duration to robustly quantify ENSO variance and extreme-event statistics in the presence of substantial natural variability[19]. Within this context, earlier multi-century time-slice experiments using the Community Earth System Model version 1.2 (CESM1.2) quantified interannual variability across Holocene climate states and compared the past estimates with coral reconstructions from the central tropical Pacific[20]. Because the changes in ENSO variability during the Holocene are relatively modest, they remain harder to detect amidst a wide range of natural variability. Building on this framework, Thirumalai et al.[21] (2024) extended the CESM1.2 analysis to the Last Glacial Maximum (LGM; ~21 thousand years ago, ka, relative to 1950 CE, hereafter) and future warming scenarios, where larger climate forcings make ENSO changes and the associated mechanisms more detectable. However, validation of past ENSO changes relied primarily on discontinuous individual foraminiferal analyses, which are less suited to resolving interannual variability and extreme-event frequency. Thus, progress requires the development of continuous, high-resolution datasets that can resolve the full spectrum of ENSO variability.

Coral oxygen-isotope records provide continuous, subseasonally-resolved archives capable of resolving ENSO amplitude and extreme-event frequency, offering a direct benchmark for evaluating ENSO behaviour across climate states[20,22-25]. Modern coral records from Kiritimati, in the Niño 3.4 region (5°N–5°S, 170°–120°W) of the central equatorial Pacific, and Vanuatu, in the southwest tropical Pacific, show that corals both within and outside ENSO's centre of action correlate with observed changes in ENSO amplitude and extreme events (Fig. 1d–f). Holocene corals extend ENSO reconstructions back hundreds to thousands of years ago, but most available archives only extend to 7 ka (Fig. 1b and Extended Data Fig. 1), largely because postglacial sea-level rise submerged most pre-to-early Holocene coral reefs, leaving relatively few accessible fossil archives (Fig. 1c). Fossil corals predating the Holocene can therefore provide a rare opportunity to evaluate model simulations of the past, as the larger glacial–interglacial climate differences during the last deglaciation make the forced ENSO changes more detectable[3].

Here we present monthly-resolved, decades-long coral oxygen-isotope records from 12 and 15 ka recovered from an island in the Republic of Vanuatu that has undergone rapid uplift, allowing easier access to older material that would normally be submerged[26-28] (Methods). Coupled with climate model simulations, these records provide the first robust model–data comparisons of the interannual variability and extreme-event frequency of ENSO under colder deglacial climate states, providing an exceedingly rare observational benchmark for evaluating the climate-state dependence of ENSO and helping constrain future projections under global warming.

Weaker ENSO in a colder world

We assessed ENSO behaviour during the Younger Dryas (YD; 12.9–11.7 ka[29]) and Heinrich Stadial 1 (HS1; 18.0–14.6 ka[30,31]) abrupt climate events by pairing our Vanuatu fossil coral records with an expanded suite of CESM1.2 time-slice simulations. These intervals coincide with abrupt reductions in Atlantic Meridional Overturning Circulation (AMOC) strength driven by large freshwater inputs from melting Northern Hemisphere ice sheets. AMOC perturbations alter Atlantic heat transport and reorganize atmospheric circulation, generating teleconnections that extend into the tropical Pacific and modulate its mean state and ENSO variability[32-39]. To evaluate ENSO responses under distinct AMOC states, we conducted new CESM1.2 experiments at 12 and 15 ka, forced with anomalous surface freshwater fluxes in the North Atlantic (Methods).

ENSO simulated in the CESM1.2 time slices strengthens monotonically from 15 ka to pre-industrial (PI) (Fig. 2a), as the Walker circulation and equatorial cold tongue weaken and the associated shoaling of the ocean mixed layer increases mechanical coupling between surface winds and ocean currents[21]. The freshwater forcing (FWF) at 12 and 15 ka strengthens ENSO relative to the temporally adjacent simulations without freshwater forcing (Fig. 2a). The mechanism enhancing ENSO during weak AMOC intervals differs from that of the glacial period and is associated with reduced annual seasonal cycle in the equatorial Pacific (Extended Data Fig. 2), consistent with the AMOC–ENSO teleconnection mechanism proposed by Timmermann et al.[35] (2007). Changes in interannual variability associated with ENSO are most pronounced in the eastern equatorial Pacific during boreal winter–spring, when the Northern Hemispheric cooling induced by AMOC slowdown extends into this region[40], and propagates into the Niño 3.4 region during spring–summer (Extended Data Fig. 2e,f). However, these AMOC-driven ENSO increases are small at 10–15% compared to the much larger 60–80% increases imposed by glacial climate forcings and boundary conditions (Fig. 2a and Extended Data Fig. 2e,f), such that ENSO in both FWF experiments remains substantially weaker than during preindustrial conditions. This contrast highlights that while AMOC weakening can amplify ENSO variability[41], the mean-state adjustments associated with deglacial climate forcing exert the dominant control leading to reduced ENSO amplitude during these intervals.

Our coral archive and CESM1.2 time-slice experiments provide a unified framework for assessing ENSO's response to deglacial climate forcing. To facilitate model–proxy comparison, tropical Pacific sea surface temperature (SST) and salinity simulated by the model were forward-modelled to coral oxygen isotopes ($\delta^{18}O_{FM}$) and perturbed with a proxy system model (PSM; $\delta^{18}O_{PSM}$). Because Vanuatu lies outside Niño 3.4 and the influence of ENSO is variable across the tropical Pacific, we assessed whether ENSO changes are detectable at this location using this model framework (Fig. 2, Extended Data Fig. 1, and Methods). Integrating site-level coral records with spatially-explicit model diagnostics allows us to isolate ENSO-driven changes from other sources of variability and quantify how ENSO variance differs between deglacial and modern climates.

Comparing fossil coral records with climate model simulations

The deglacial coral records and CESM1.2 simulations agree that there is a basin-wide weakening of interannual variability in a colder world, providing independent validation of reduced ENSO intensity under glacial conditions. Both the deglacial coral records and the southwest Pacific (SWP) $\delta^{18}O_{PSM}$, representing simulated Vanuatu coral records, show a coherent reduction in interannual variance relative to the late-Holocene baseline (Fig. 2b). Within the Niño 3.4 region, CESM1.2 time slices align with previously published Kiritimati coral records, which show reduced mid-Holocene variance (Fig. 2c), albeit with a 10–20% smaller signal, relative to coral estimates[20,22]. These site-specific reductions in interannual variance mirror the modelled decrease in ENSO amplitude (Fig. 2a).

To examine how forced ENSO changes are represented in tropical Pacific coral records, we compare the spatial structure of simulated total interannual variance and its ENSO-explained component, estimated by linear regression onto the Niño 3.4 SST index (Fig. 3). Comparing total interannual and ENSO-explained variances allows us to assess whether the observed changes in reconstructed interannual variance primarily reflect ENSO or other sources of climate variability. Across all time slices, the percent of total interannual variance change that is explained by ENSO ranges from a low of ~50 during the Holocene to a high of ~70 during the deglacial. These results indicate that basin-wide changes in interannual variability are dominated by ENSO dynamics rather than by non-ENSO sources of variability, and a larger proportion of interannual variance is explained by ENSO when the change in ENSO amplitude is larger (Fig. 3 and Extended Data Fig. 1c–p).

During the deglaciation, total interannual variance at SWP decreases by 33–40% relative to the PI control, and 34–50% of that reduction is attributable to ENSO. The remaining variance changes likely reflect local processes or remote influences unrelated to ENSO. This result demonstrates that Vanuatu corals are recorders of forced ENSO changes. The early-to-mid Holocene reductions in total interannual variance are only 4–17%, and the ENSO-explained portion of 0–11% is minimal, making forced ENSO signals difficult to detect in coral records from this interval. This muted Holocene response at SWP reflects a broader basin-wide pattern: across the tropical Pacific, site-level differences in ENSO sensitivity produce substantial spatial heterogeneity in Holocene ENSO reconstructions, often obscuring weak forced signals – a challenge highlighted by Cobb et al.[22] (2013). The emergence of a clear ENSO-dominated signal during the deglaciation underscores that large, basin-wide reductions in interannual variability rise above this spatial heterogeneity and become detectable in individual coral records.

Extreme El Niño frequency across climate regimes

Extreme El Niño frequency, defined relative to the PI-control percentile threshold, scales linearly with ENSO amplitude across the CESM1.2 time slices, revealing a robust linear relationship (m = 0.099 events century^{-1} % variance change^{-1}, R = 0.995) between overall variability and extreme-event behaviour[21] (Fig. 4a; Methods). Deglacial simulations, which exhibit the weakest ENSO amplitude, produce 0–1 extreme events century^{-1}, whereas early-to-mid Holocene simulations indicate 4–5 events century^{-1}. Extreme-event frequency increases substantially under 2xCO_2-forcing, more than doubling relative to PI.

To investigate whether this modelled relationship between ENSO amplitude and extreme-event frequency (Fig. 4a) can help interpret the coral records, we next examined the relationship at the local scale. Local extreme events at Vanuatu and Kiritimati also scale linearly with total interannual variance in simulated $\delta^{18}O_{PSM}$ anomalies (SWP: m = 0.088 events century^{-1} % variance change^{-1}, R = 0.964; CEP: m = 0.094 events century^{-1} % variance change^{-1}, R = 0.999), and the corresponding coral $\delta^{18}O$ relationships (Vanuatu: m = 0.199 events century^{-1} % variance change^{-1}, R = 0.967; Kiritimati: m = 0.093 events century^{-1} % variance change^{-1}, R = 0.776) agree with these model-based results (Fig. 4b,c; Methods). The local linear relationships demonstrate that local extremes respond similarly to extreme El Niño across climate states. However, local extremes can arise from either ENSO-driven anomalies or non-ENSO processes, making it essential to determine their source. To isolate the ENSO-driven subset, we diagnosed whether each local extreme occurs with extreme El Niño in the CESM1.2 simulations (Methods). At both sites, the frequency of coeval extremes increases with total interannual variance (Fig. 4d,e), confirming that most local extremes are tied to extreme El Niño events rather than to independent regional processes. Proxy-system noise in the age modelling dampens this relationship at Kiritimati because age uncertainty smears the timing of sharp, event-scale $\delta^{18}O$ anomalies[42], whereas Vanuatu's broader, rainfall-driven anomalies are far less sensitive to age offsets. The local variance–extreme-event relationship reinforces the interpretation that both sites record the basin-wide expression of ENSO extremes, underscoring that total interannual variance reliably predicts extreme-event behaviour across climate states.

Model validation and future projections of ENSO

Across all metrics of interannual variability presented in Fig. 4, a consistent climate-regime structure emerges: deglacial intervals cluster at low SSTA variance changes of -75 to -55% and low extreme-event frequency of 0–1 century^{-1}, Holocene intervals occupy an intermediate regime with SSTA variance changes of -35 to 0% and frequency of 4–7 century^{-1}, and the 2xCO_2 simulation defines a distinct regime with high SSTA variance change of 75%, and high extreme frequency of 14–15 century^{-1}. This tripartite structure indicates that ENSO responds systematically to large-scale changes in boundary conditions and radiative forcings, with muted responses during the Holocene and much larger responses during the deglaciation and under 2xCO_2. Because the deglacial and Holocene intervals span a wide range of background climate states, they provide a powerful out-of-sample test for emergent constraints on future ENSO amplitude and extreme-event behaviour. The deglacial coral records fall within the modelled low-variance, low-extreme-frequency regime and align with marine-sediment evidence for weak ENSO intensity[41] and a reduced relative frequency of extreme El Niño events[21], providing an independent benchmark for evaluating model behaviour. Notably, CESM1.2 simulates a larger ENSO reduction during the deglaciation than during the LGM[21], even when the reduced AMOC acts to strengthen ENSO, suggesting that the deglacial interval offers a particularly sensitive window for detecting forced changes in interannual variability of the tropical Pacific over the past 21 ka. Together with the freshwater-forced simulations, the new coral results reduce uncertainty in emergent constraints, linking stronger ENSO variability to more frequent extreme El Niño events in a warming climate, and represent a key step toward building a more complete model hierarchy for evaluating palaeo-ENSO dynamics across diverse climate states.

The spatial structure of interannual variance changes reveals how ENSO regulates year-to-year climate variability across the tropical Pacific under different background climate states (Fig. 2). Despite spanning a wide range of mean-state conditions, the deglacial intervals we sampled – HS1 and YD – remain confined to low-variance regimes, with extreme El Niño events becoming progressively rarer in older, colder climate states, although ENSO behaviour during the Bølling Allerød (14.6–12.9 ka) remains poorly constrained. Our coral records show that these past ENSO regimes persisted despite large changes in ice volume, radiative forcing[43], and ocean circulation[31], with muted responses during the Holocene and substantially weaker ENSO during the deglaciation. In contrast, the 2xCO_2 simulation departs sharply from the late-Quaternary variability envelope. This departure aligns with work showing that greenhouse forcing can shift the spatial pattern and frequency of ENSO events beyond the range of late-Quaternary variability[44], even while the underlying variance–extreme-event relationship remains consistent across past climate states.

An important implication of our results is that the spatial footprint of ENSO extremes expands nonlinearly in a warmer world. Relative to the modest deglacial-to-present increase, the present-to-2xCO_2 response at Vanuatu represents a much larger shift, yielding extreme-event frequencies comparable to those in Niño 3.4 and indicating disproportionately strong future amplification outside the ENSO centre[45]. This behaviour is consistent with projections of enhanced ENSO teleconnections and broader Pacific-wide impacts under greenhouse forcing[1,2,6,46]. Recent observational evidence of ongoing AMOC weakening[47] suggests that major background-state adjustments that could influence ENSO dynamics may already be underway in the modern climate system. Yet our simulations indicate that AMOC-related changes yield only modest increases in ENSO variability, whereas greenhouse gas (GHG) forcing produces far stronger amplification. Assuming linearity of ENSO's response to climate forcings, CESM1.2 therefore points to GHG-driven mean-state adjustments as the primary cause of future increases in ENSO amplitude and extreme-event frequency. Inter-model differences in AMOC response nonetheless shape future climate projections[48], underscoring the importance of accurately representing AMOC–Pacific teleconnections when evaluating forced changes in ENSO. The coral–model agreement across past climate states in our study strengthens confidence in these projections, suggesting that future ENSO amplification will produce more widespread and severe impacts across the tropical Pacific than observed in the late Holocene under SSP2-4.5 to SSP5-8.5 forcing.

Taken together, the deglacial and Holocene coral–model comparisons show that past climate states provide essential leverage for emerging constraints on future ENSO behaviour, revealing how ENSO responds to large-scale forcing in ways not observable in the modern record alone. Although uncertainties remain in the magnitude of future ENSO amplification[3,4,8,11] and in the regional expression of extreme events[1,2,6], the agreement between coral records and model behaviour across past climate states (Figs. 3 and 4) provides a rare observational benchmark for assessing model projections. The emergence of a high-variance, high-extreme-frequency regime under 2xCO_2 suggests that anthropogenic forcing may reorganize ENSO variability beyond the range of late-Quaternary experience. By demonstrating how extreme-event behaviour scales with total interannual variance across diverse climate backgrounds, our coral–model synthesis offers a framework for interpreting future ENSO changes and anticipating the broader climatic impacts of a more variable and extreme tropical Pacific.

Main references

1. Cai, W. *et al.* Increasing frequency of extreme El Niño events due to greenhouse warming. *Nature Climate Change* **4**, 111–116 (2014).
2. Wang, B. *et al.* Historical change of El Niño properties sheds light on future changes of extreme El Niño. *Proc Natl Acad Sci U S A* **116**, 22512–22517 (2019).
3. Brown, J. R. *et al.* Comparison of past and future simulations of ENSO in CMIP5/PMIP3 and CMIP6/PMIP4 models. *Climate of the Past* **16**, 1777–1805 (2020).
4. Cai, W. *et al.* ENSO Response to Greenhouse Forcing. in *Geophysical Monograph Series: El Niño Southern Oscillation in a Changing Climate* 289–307 (Wiley, 2020).
5. Maher, N., Matei, D., Milinski, S. & Marotzke, J. ENSO Change in Climate Projections: Forced Response or Internal Variability?. *Geophysical Research Letters* **45**, 86 (2018).
6. Holbrook, N. J. *et al.* A global assessment of marine heatwaves and their drivers. *Nature Communications* **10**, 2624 (2019).
7. DeLong, K. L., Quinn, T. M., Taylor, F. W., Lin, K. & Shen, C.-C. Sea surface temperature variability in the southwest tropical Pacific since AD 1649. *Nature Climate Change* **2**, 799–804 (2012).
8. Beobide-Arsuaga, G., Bayr, T., Reintges, A. & Latif, M. Uncertainty of ENSO-amplitude projections in CMIP5 and CMIP6 models. *Climate Dynamics* **56**, 3875–3888 (2021).
9. Fredriksen, H., Berner, J., Subramanian, A. C. & Capotondi, A. How Does El Niño–Southern Oscillation Change Under Global Warming—A First Look at CMIP6. *Geophysical Research Letters* **47**, 123 (2020).
10. Heede, U. K. & Fedorov, A. V. Towards understanding the robust strengthening of ENSO and more frequent extreme El Niño events in CMIP6 global warming simulations. *Climate Dynamics* **61**, 3047–3060 (2023).

11. IPCC. *Climate Change 2023: Synthesis Report. Contribution of Working Groups I, II and III to the Sixth Assessment Report of the Intergovernmental Panel on Climate Change* (Intergovernmental Panel on Climate Change (IPCC), 2023).

12. Zhu, J. *et al.* Reduced ENSO variability at the LGM revealed by an isotope-enabled Earth system model. *Geophysical Research Letters* **44**, 6984–6992 (2017).

13. Han, T., de Winter, N. J., Liu, C., Zhao, N. & Yan, H. Quantifying Past ENSO Variability From Tridacna δ18O Using a Pseudo-Proxy Baseline Approach. *Paleoceanography and Paleoclimatology* **41**, 0 (2026).

14. Huang, J. *et al.* Persistent El Niño-like conditions over the western Pacific during the Bølling–Allerød interstadial. *Communications Earth & Environment* **7**, 0 (2025).

15. Lu, W. *et al.* Warmer shallow Atlantic during deglaciation and early Holocene due to weaker overturning circulation. *Nature Geoscience* **18**, 787–792 (2025).

16. Yseki, M. *et al.* El Niño–Southern Oscillation strengthened by North Atlantic Iceberg discharge during Heinrich stadial 1. *Communications Earth & Environment* **7**, 0 (2026).

17. Pontes, G. M., da Silva Dias, P. L. & Menviel, L. Rapid communication: Nonlinear sensitivity of the El Niño–Southern Oscillation across climate states. *Climate of the Past* **21**, 1079–1091 (2025).

18. Tiwari, S. *et al.* Mid-Holocene El Niño Southern Oscillation variability reduced by northern African vegetation changes in climate models. *Communications Earth & Environment* **6**, 0 (2025).

19. Wittenberg, A. T., Rosati, A., Delworth, T. L., Vecchi, G. A. & Zeng, F. ENSO Modulation: Is It Decadally Predictable?. *Journal of Climate* **27**, 2667–2681 (2014).

20. Lawman, A. E. *et al.* Unraveling forced responses of extreme El Niño variability over the Holocene. *Science Advances* **8**, eabm4313 (2022).

21. Thirumalai, K. *et al.* Future increase in extreme El Niño supported by past glacial changes. *Nature* **634**, 374–380 (2024).

22. Cobb, K. M. *et al.* Highly Variable El Niño–Southern Oscillation Throughout the Holocene. *Science* **339**, 67–70 (2013).

23. Grothe, P. R. *et al.* Enhanced El Niño–Southern Oscillation Variability in Recent Decades. *Geophysical Research Letters* **47**, e2019GL083906 (2020).

24. Lawman, A. E. *et al.* A century of reduced ENSO variability during the Medieval Climate Anomaly. *Paleoceanography and Paleoclimatology* **35**, e2019PA003742 (2020).

25. McGregor, H. V. *et al.* A weak El Niño/Southern Oscillation with delayed seasonal growth around 4,300 years ago. *Nature Geoscience* **6**, 949–953 (2013).

26. Corrège, T. *et al.* Interdecadal variation in the extent of South Pacific tropical waters during the Younger Dryas event. *Nature* **428**, 927–929 (2004).

27. Taylor, F. W., Edward, R. L., Wasserburg, G. J. & Frohlich, C. Seismic recurrence intervals and timing of aseismic subduction inferred from emerged corals and reefs of the central Vanuatu (New Hebrides) frontal arc. *Journal of Geophysical Research: Solid Earth* 393–408 (1990).

28. Voosen, P. The coral chronicles. *Science* **383**, 472–477 (2024).

29. Alley, R. B. The Younger Dryas cold interval as viewed from central Greenland. *Quaternary Science Reviews* **19**, 213–226 (2000).

30. Denton, G. H. *et al.* The Last Glacial Termination. *Science* **328**, 1652–1656 (2010).

31. McManus, J. F., Francois, R., Gherardi, J. M., Keigwin, L. D. & Brown-Leger, S. Collapse and rapid resumption of Atlantic meridional circulation linked to deglacial climate changes. *Nature* **428**, 834–837 (2004).

32. Liu, W., Pinto, D. D. C., Fedorov, A. & Zhu, J. The Impacts of a Weakened Atlantic Meridional Overturning Circulation on ENSO in a Warmer Climate. *Geophysical Research Letters* **50**, e2023GL103025 (2023).

33. Merkel, U., Prange, M. & Schulz, M. ENSO variability and teleconnections during glacial climates. *Quaternary Science Reviews* **29**, 86–100 (2010).

34. Orihuela-Pinto, B., England, M. H. & Taschetto, A. S. Interbasin and interhemispheric impacts of a collapsed Atlantic Overturning Circulation. *Nature Climate Change* **12**, 558–565 (2022).

35. Timmermann, A. *et al.* The Influence of a Weakening of the Atlantic Meridional Overturning Circulation on ENSO. *Journal of Climate* **20**, 4899–4919 (2007).

36. Williamson, M. S. *et al.* Effect of AMOC collapse on ENSO in a high resolution general circulation model. *Climate Dynamics* **50**, 2537–2552 (2018).

37. Yang, Y. *et al.* Weakened Atlantic Meridional Overturning Circulation Contributes to Opposite Responses of ENSO and the Atlantic Niño/Niña to Greenhouse Warming. *Geophysical Research Letters* **52**, 1 (2025).

38. Zhang, R. & Delworth, T. L. Simulated Tropical Response to a Substantial Weakening of the Atlantic Thermohaline Circulation. *Journal of Climate* **18**, 1853–1860 (2005).

39. Zhang, R. *et al.* A Review of the Role of the Atlantic Meridional Overturning Circulation in Atlantic Multidecadal Variability and Associated Climate Impacts. *Reviews of Geophysics* **57**, 316–375 (2019).

40. Xie, S.-P., Okumura, Y., Miyama, T. & Timmermann, A. Influences of Atlantic climate change on the tropical Pacific via the Central American Isthmus. *Journal of Climate* **21**, 3914–3928 (2008).

41. Glaubke, R. H. *et al.* An Inconsistent ENSO Response to Northern Hemisphere Stadials Over the Last Deglaciation. *Geophysical Research Letters* **51**, 1 (2024).

42. Lawman, A. E. *et al.* Developing a coral proxy system model to compare coral and climate model estimates of changes in paleo-ENSO variability. *Paleoceanography and Paleoclimatology* **35**, e2019PA003836 (2020).

43. Shakun, J. D. *et al.* Global warming preceded by increasing carbon dioxide concentrations during the last deglaciation. *Nature* **484**, 49–54 (2012).

44. Yeh, S. *et al.* ENSO Atmospheric Teleconnections and Their Response to Greenhouse Gas Forcing. *Reviews of Geophysics* **56**, 185–206 (2018).

45. Tindall, J. C., Haywood, A. M. & Thirumalai, K. Modeling the stable water isotope expression of El Niño in the Pliocene: Implications for the interpretation of proxy data. *Paleoceanography* **32**, 881–902 (2017).

46. Power, S., Delage, F., Chung, C., Kociuba, G. & Keay, K. Robust twenty-first-century projections of El Niño and related precipitation variability. *Nature* **502**, 541–545 (2013).

47. Xing, Q. *et al.* Meridionally consistent decline in the observed western boundary contribution to the Atlantic Meridional Overturning Circulation. *Science Advances* **12**, eadz7738 (2026).

48. Bellomo, K., Angeloni, M., Corti, S. & von Hardenberg, J. Future climate change shaped by inter-model differences in Atlantic meridional overturning circulation response. *Nature Communincations* **12**, 3659 (2021).

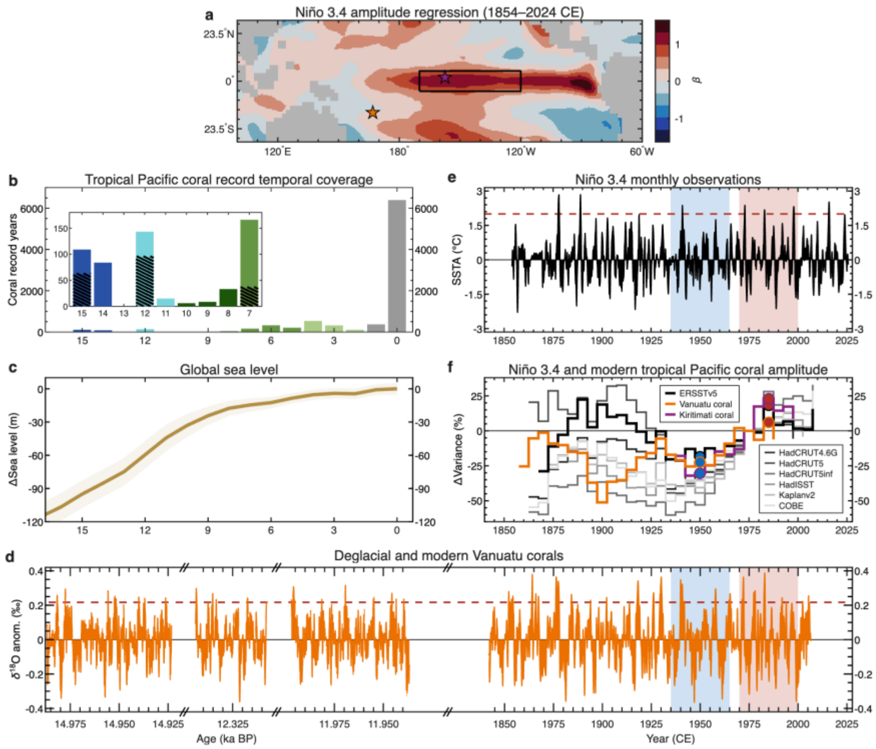

Fig. 1 | Tropical Pacific interannual variability and subannually resolved coral record availability since the last deglaciation. a, Observed regression of running standard deviations of tropical Pacific sea surface temperature anomalies (SSTA) from the Extended Reconstructed Sea Surface Temperature version 5 (ERSSTv5) onto the Niño 3.4 region (black rectangle; 5°S–5°N, 170–120°W). Pentagrams denote coral sites in Vanuatu (orange) and Kiritimati (magenta). **b**, Temporal coverage of subannually resolved tropical Pacific coral records (see Supplementary Table 1), grouped by overlapping number of years interval^{-1}. Inset hatching depicts this study's coral contribution. **c**, Global sea level changes relative to modern from ocean sediment cores[49]. Shading represents the ±1σ uncertainty range. **d**, Monthly $\delta^{18}O$ anomalies from newly acquired deglacial corals (dated to 15.0 ka, 12.3 ka, and 12.0 ka) and published modern corals (1843–2007 CE) from Vanuatu. **e**, ERSSTv5 monthly SSTA (1854–2024 CE) in the Niño 3.4 region. **f**, Interannual variance percent changes relative to 1960–1989 CE, computed from Niño 3.4 SSTA in seven observational products (black and grey lines) and modern monthly $\delta^{18}O$ anomalies from Vanuatu (orange) and Kiritimati (purple) corals. Shaded intervals in **c**,**d**) represent historically weaker (blue, 1935–1964 CE) and stronger (pink, 1970–1999 CE) El Niño–Southern Oscillation (ENSO) periods. Dashed red lines depict extreme El Niño thresholds at the 93rd percentile of November–December–January averaged (NDJ) coral $\delta^{18}O$ anomalies in Vanuatu (**d**) and 2 °C in Niño 3.4 (**e**). In **f**), blue (red) circles are variance changes for weaker (stronger) periods indicated by light blue (pink) shading in **d**,**e**.

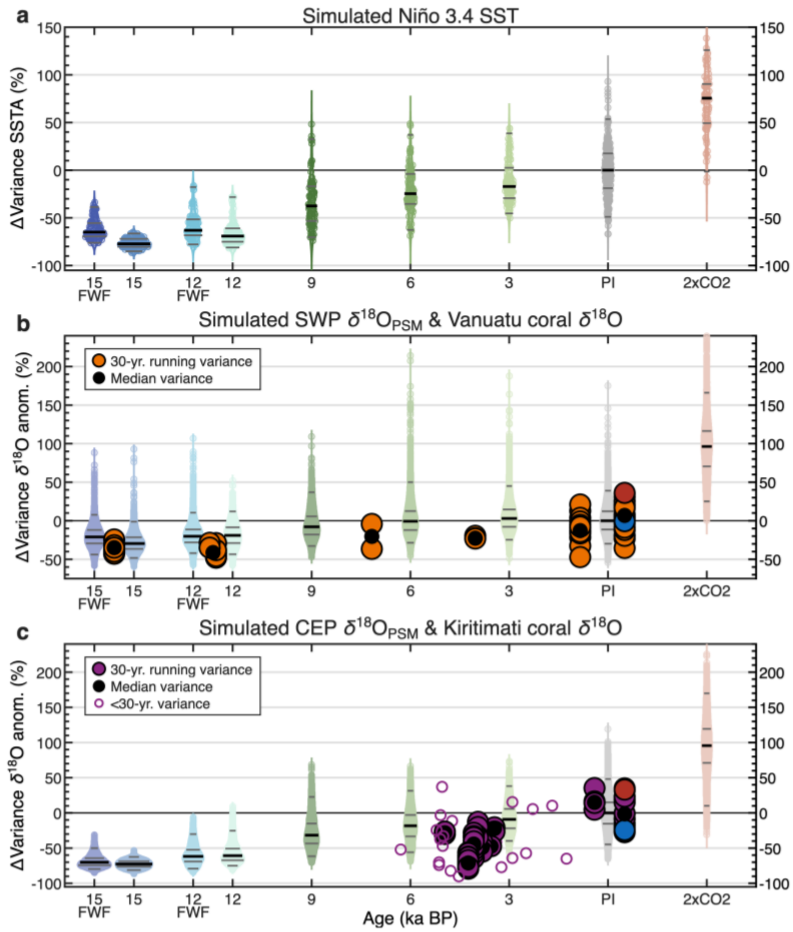

Fig. 2 | Tropical Pacific interannual variance changes since the last deglaciation and under an atmospheric CO_2 doubling. a–c, Interannual variance percent changes in simulated Niño 3.4 SSTA (**a**), simulated southwest tropical Pacific (SWP) proxy-system-modelled $\delta^{18}O$ ($\delta^{18}O_{PSM}$; violin plots) and Vanuatu coral $\delta^{18}O$ (colored circles) anomalies (**b**), and simulated central equatorial Pacific (CEP) $\delta^{18}O_{PSM}$ (violin plots) and Kiritimati coral $\delta^{18}O$ (colored circles) anomalies (**c**). Violin plots depict 30-year running variance changes; thick black lines on violin plots are medians, and thin grey lines are 2.5^{th}, 25^{th}, 75^{th}, and 97.5^{th} percentiles. Coral records show 30-year running variance changes (filled colored circles), median variance changes (filled black circles), and under-30-year variance changes in **c**) (unfilled colored circles). Blue (red) circles in modern corals indicate weaker (stronger) ENSO periods depicted in Fig. 1f. A single median is computed for combined running variance changes in 12.0- and 12.3-ka corals. Modern, 12.0-ka, 12.3-ka, and 15.0-ka corals are shifted temporally for visualization. Model-based changes are relative to the PI control and coral-based changes are relative to records dated to within 1,500 years of the modern era. Percent ranges vary across panels.

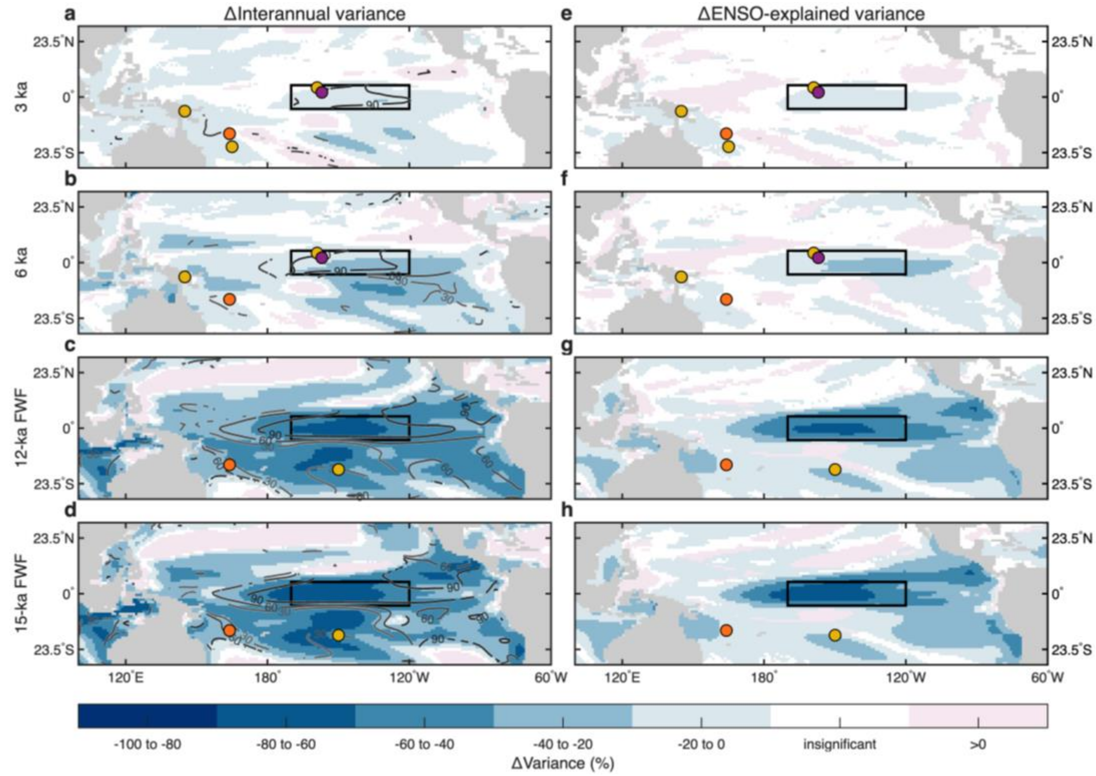

Fig. 3 | Simulated tropical Pacific interannual and ENSO-explained variance changes since the last deglaciation. a–d, Interannual variance percent changes from the pre-industrial (PI) control of simulated forward-modelled (FM) $\delta^{18}O$ ($\delta^{18}O_{FM}$) anomalies at 3 ka (**a**), 6 ka (**b**), 12-ka freshwater forcing (FWF) (**c**), and 15-ka FWF (**d**). Grey contours depict the ENSO-explained variance change as a percentage of the interannual variance change where both are significant. **e**–**h**, ENSO-explained variance percent changes of $\delta^{18}O_{FM}$ anomalies at 3 ka (**e**), 6 ka (**f**), 12-ka FWF (**g**), and 15-ka FWF (**h**). White regions depict insignificant changes (Methods). Colored circles represent sites – Vanuatu (orange), Kiritimati (purple) and other locations (gold) – with subannually resolved coral records dated to within 1,500 years of both the modern era and the given time slices. Black rectangle represents the Niño 3.4 region.

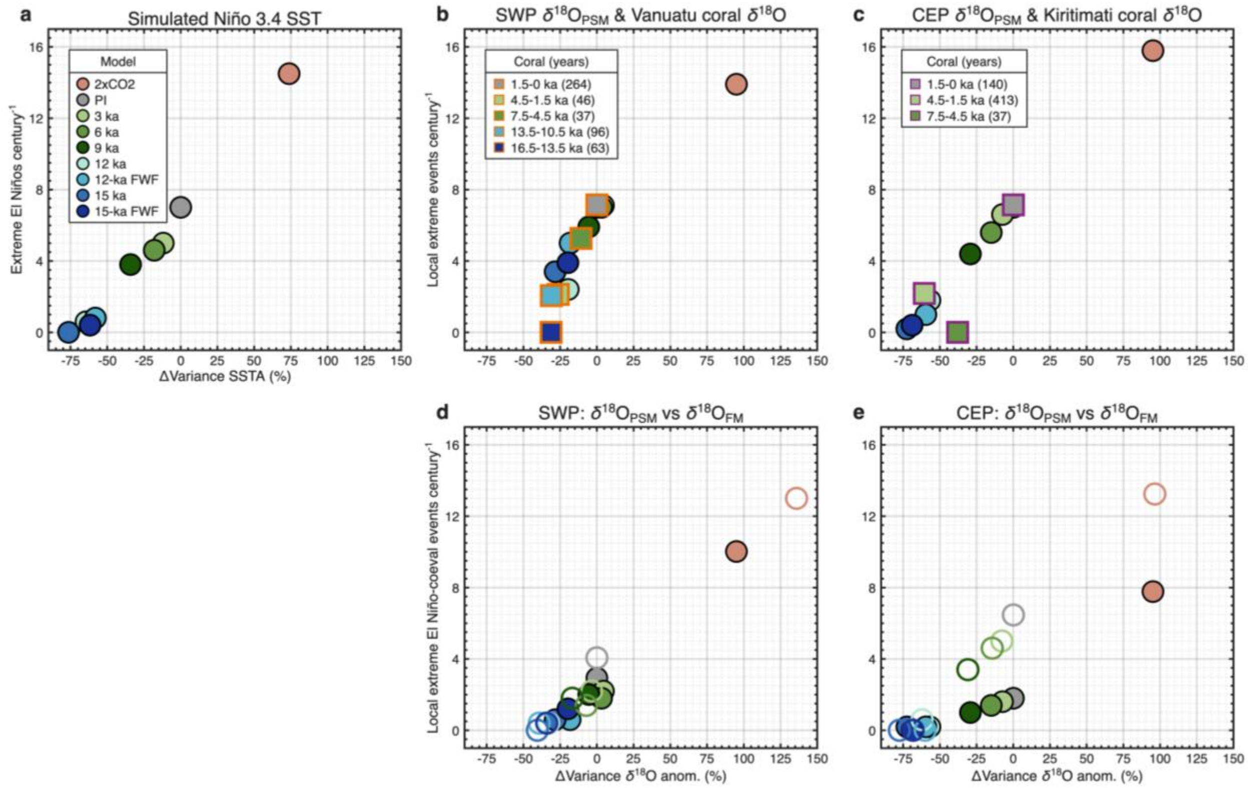

Fig. 4 | Relationship of extreme-event frequency to changes in interannual variance since the last deglaciation and under an atmospheric CO_2 doubling. a, Extreme El Niño event frequency (century^{-1}) and changes in interannual Niño 3.4 SSTA variance (% change from the PI control). Legend applies to all panels. **b**,**c**, Relationship between local extreme-event frequency and interannual variance in simulated SWP $\delta^{18}O_{PSM}$ and Vanuatu coral $\delta^{18}O$ anomalies (**b**) and simulated CEP $\delta^{18}O_{PSM}$ and Kiritimati coral $\delta^{18}O$ anomalies (**c**). Coral records are grouped by age into intervals and only include records 30 years and longer (Methods). Parenthesized values in legends depict number of years in each age interval. **d**,**e**, Relationship between the frequency of local extremes coeval with extreme El Niño and interannual variance in SWP $\delta^{18}O_{FM}$ and $\delta^{18}O_{PSM}$ anomalies (±1 year; see Methods) (**d**) and CEP $\delta^{18}O_{FM}$ and $\delta^{18}O_{PSM}$ anomalies (±1 year) (**e**). $\delta^{18}O_{PSM}$ ($\delta^{18}O_{FM}$) extreme-event frequencies are depicted by filled (open) markers.

Methods

Coral archives and suitability for ENSO reconstruction

Tropical Pacific *Porites* corals can provide monthly resolution, enabling removal of the annual cycle and isolation of interannual ENSO-band variability. Their ages can be determined with <1% uncertainty using uranium–thorium (U–Th) disequilibrium dating, allowing precise placement of fossil records within deglacial climate events. Vanuatu offers a uniquely advantageous setting for recovering deglacial corals: rapid tectonic uplift in southwest Espiritu Santo (5–7 mm yr^{-1})[27] elevates formerly submerged deglacial coral terraces to shallow depths (1–15 m), permitting direct sampling of corals that originally grew 10–130 m below modern sea level. These attributes make uplifted Vanuatu corals exceptionally well suited for reconstructing ENSO strength and extreme-event frequency across the last 15 thousand years (ka) before present (BP, before 1950).

Vanuatu coral collection and uranium-thorium dating

To recover fossil corals spanning deglacial and Holocene intervals, we targeted uplifted terraces along the coastlines of Araki Island and Tanovusvus Village, southwest Espiritu Santo Island, in the Republic of Vanuatu (Extended Data Fig. 3). Rapid uplift in this region exposes formerly submerged deglacial corals at shallow depths, enabling in situ sampling of material that originally grew tens of meters below modern sea level. Fossil *Porites* corals were collected in 2005, 2011, and 2019 using chainsaw-mounted or portable land-drill coring systems. Core 05-AR-I, collected *in situ* on Araki in 2005, and core 11-TVS-B, collected *in situ* at Tanovusvus in 2011, were drilled with a Stihl chainsaw equipped with a Pomeroy Gear-Reduced Core Drill and diamond coring bits. Specimens 19-TV-K, collected *in situ* from a cliff face, and 19-TV-J, collected from an unattached boulder at the base of the same cliff, were extracted with hammers and chisels at Tanovusvus in 2019. It is likely that the 19-TV-J boulder was dislodged from above the cliff containing 19-TV-K. Core 19-TV-2 was drilled *in situ* at Tanovusvus in 2019 with a Tech2000 Ultra-Portable Land Drill prototype equipped with a Tungsten carbide coring bit.

05-AR-I was U–Th dated on a Finnigan Element magnetic sector inductively coupled plasma–mass spectrometer (ICP-MS)[50] at the Department of Earth Sciences, University of Minnesota (Supplementary Table 2). 11-TVS-B, 19-TV-J, 19-TV-K, and 19-TV-2 were U–Th dated on a Thermo Electron Neptune multicollector ICP-MS (MC-CIP-MS)[51] at the High-precision Mass Spectrometry and Environmental Change Laboratory, National Taiwan University. Half-lives of ^{234}U[52] and other U-Th nuclides in Cheng et al.[53] (2013) were used for ^{230}Th age calculation. Uncertainties in isotopic data and ^{230}Th dates, relative to AD 1950, are given at the two-sigma (2σ) level or two standard deviations of the mean ($2\sigma_m$) unless otherwise noted. An assumed initial $^{230}Th/^{232}Th$ atomic ratio of $(4 \pm 2) \times 10^{-6}$ was applied for age correction. The results are given in Supplementary Table 2.

Screening for diagenesis

All new corals were screened for diagenesis using scanning electron microscopy (SEM) and X-ray diffraction (XRD). Coral slivers taken from the top and bottom of each core/specimen were rinsed in distilled water and dried. One half of each sliver was reserved for SEM screening, and the other half was powdered for XRD analysis. Secondary aragonite screening was performed on a JEOL JSM-6490LV SEM, which showed no-to-minimal secondary aragonite needles ranging from 1 to 7μm in length (Extended Data Figs. 4–8). Screening for calcite was performed on a Bruker D8 Advance XRD with JADE pattern processing software. Powdered samples were analyzed with Cu–Kα radiation (45 kV, 40 mA) from 20 to 40° 2q in 0.5°/minute steps to determine the presence of [111] aragonite (3.40 Å), [102] aragonite (3.27 Å), and [104] calcite

(3.04 Å) peaks. XRD results showed no calcite in all samples. Combined with the determined initial d^{234}U values of 141–148 and ^{238}U contents of 2.3–2.6 ppm, these lines of evidence demonstrate that the Holocene and deglacial fossil corals used are pristine.

X-radiography, growth axis sampling, and δ^{18}O analysis

Annual density banding was imaged on 5-mm thick coral slabs using X-radiography to determine optimal sampling paths along the maximum growth axis. The high temporal resolution of *Porites* corals allows sampling at 12–14 points per annual band, sufficient to isolate ENSO-band variability once the annual cycle is removed. Slabs were cleaned and micromilled following established protocols cited in Lawman et al.[24] (2020). Slabs were X-ray imaged again after sampling to ensure adherence to the optimal sampling paths.

δ^{18}O values for corals 05-AR-I and 11-TVS-B were measured using a Thermo Mat 253 gas isotope ratio mass spectrometer (IRMS) coupled with a Kiel IV Carbonate Device at the Stable Isotope Geosciences Facility, Texas A&M University. NBS-19 and IAEA-603 standards used to monitor short-term precision for δ^{18}O are consistent with long-term precision of this instrumental setup (±0.06‰, 1σ). δ^{18}O values for corals 19-TV-J, 19-TV-K, and 19-TV-2 were measured using a Thermo Mat 253+ gas IRMS coupled with a Kiel IV Carbonate Device at the Paleo^2 Laboratory, University of Arizona. IAEA-603 standards used to monitor short-term precision for δ^{18}O are consistent with long-term precision of this instrumental setup (±0.05‰, 1σ).

Age modeling of the Vanuatu coral δ^{18}O records was carried out using a climatology-anchored approach based on forward-modelled δ^{18}O from two ocean reanalyses – the European Centre for Medium-Range Weather Forecasts Ocean Reanalysis 20C[54] (ORA-20C; 1900–2009 CE) and the Simple Ocean Data Assimilation[55] (SODA; 1871–2010 CE) – together with one observational product, the Extended Reconstructed Sea Surface Temperature version 5[56]

(ERSSTv5; 1854–2025 CE) combined with Delcroix sea surface salinity[57] (Delcroix; 1950–2009 CE) (see Supplementary Table 3). Forward-modelled $\delta^{18}O$ was derived from sea surface temperature (SST) and sea surface salinity (SSS) fields using the $\delta^{18}O_{seawater}$ relationships of LeGrande and Schmidt[58] (2006) and Thompson et al.[59], following the climatology-anchored framework of Lawman et al.[42] (2020). These datasets indicate that the climatological coolest (warmest) month at Vanuatu is August (February), and these seasonal anchors were applied consistently across fossil and modern records. All previously published modern Vanuatu coral records were incorporated as published, with two anomaly versions generated: one with the 1961–1990 CE climatology removed for comparison with observational products (Fig. 1d,f), and one with the full-record climatology removed for comparison with paleo-coral records and CESM1.2 simulations (Figs. 2b and 4b).

Published Kiritimati coral records and age-model processing

We reprocessed published modern coral records from Kiritimati using the age-model algorithm of Lawman et al.[42] (2020) to minimize changes in variance through time that arise when modern and fossil corals are age-modelled differently. Modern coral records are often stretched and squeezed to match monthly observations, which increases interannual variance; however, this procedure cannot be applied to paleorecords because no instrumental analogs exist for those intervals. Modern Kiritimati corals were calendared using the same climatology-anchored algorithm as the Vanuatu corals[42], with forward-modelled $\delta^{18}O$ derived from the ORA-20C, SODA, and ERSSTv5+Delcroix datasets. These annual cycles indicate that the climatological coolest (warmest) month in Kiritimati is February (June) (Extended Data Fig. 9b), and these anchors were applied consistently across both modern and fossil records (see Supplementary Table 4).

We compiled four published modern Kiritimati coral records, each subannually resolved and archived with raw depth data. These individual modern coral records were reprocessed with the age-model algorithm and then spliced to form a continuous modern Kiritimati coral compilation (Extended Data Fig. 9a). Finally, we generated two versions of monthly coral $\delta^{18}O$ anomalies: one with the 1961–1990 CE climatology removed for comparison with observational products (Fig. 1f), and one with the full-record climatology removed for comparison with paleo-coral records and CESM1.2 simulations (Figs. 2c and 3c).

Observational SST datasets

We use the ERSSTv5 dataset[56] as a reference to assess historical ENSO amplitude and extreme El Niño events (Fig. 1a,e,f). ERSSTv5 provides monthly global spatially complete SST on a 2° grid from 1854 through the present. Incorporation of new, high-quality observations, improved bias corrections, and reduced spatial smoothing in ERSSTv5 resulted in a better representation of ENSO[60]. In total, we compare long-term changes in ENSO amplitude across seven observational datasets, including Centennial *in situ* Observation-Based Estimates[61] (COBE), ERSSTv5[56], Hadley Centre/Climatic Research Unit Temperature versions 4.6[62,63] (HadCRUT4.6), 5[64] (HadCRUT5), and 5-infilled (HadCRUT5inf), Hadley Centre Global Sea Ice and Sea Surface Temperature[65] (HadISST), and the Kaplan Sea Surface Temperature Analysis version 2[66] (KaplanSSTv2). These are shown in Fig. 1f, expressly to highlight multi-observational comparisons in ENSO amplitude in both the diversity in the early 20th century and the increasing trend into the late 20th century. Each of the products compared in Fig. 1f shows a trend of weaker-to-stronger ENSO in the mid- to late 20th century, and Brown–Forsythe testing shows that the SST anomaly (SSTA) variances in the weaker (1935–1964 CE) and stronger (1970–1999 CE) intervals within each dataset are statistically different at a 1% significance level.

CESM1.2 time slice simulations and forward-modeling framework

Coral records are compared with a suite of numerical simulations conducted with CESM1.2 for eight distinct past intervals, each 3 ka apart, from the Last Glacial Maximum (21 ka BP) to pre-industrial conditions (PI control; 0.1 ka BP), as well as for a future scenario. CESM1.2 consists of the atmosphere, land, ocean, and sea ice components linked via a flux coupler, and we use the version with a nominal 1° resolution for the ocean and sea ice components and a 2° resolution for the atmosphere and land components. CESM1.2 reproduces key observed ENSO characteristics in the PI-control simulation, including the diversity in the pattern and temporal evolution of individual events, as well as the asymmetry between El Niño and La Niña[67-69]. Nevertheless, ENSO amplitude is overestimated, and the oceanic and atmospheric anomaly patterns extend too far westward relative to observations. Boundary conditions and radiative forcings used for the CESM1.2 time slice simulations are summarized in Supplementary Table 5 and explained in detail in Thirumalai et al.[21] (2024). In each experiment, the model is integrated over 400–1500 years after reaching the equilibrium climate to obtain stable statistics of ENSO (Supplementary Table 5).

These CESM1.2 time slice simulations from Thirumalai et al.[21] (2024) do not use freshwater forcing. However, the new deglacial corals recovered from Vanuatu grew during abrupt climate events, namely the Younger Dryas (~12.9–11.7 ka) and Heinrich Stadial 1 (~18–14.6 ka), when a sudden flux of freshwater reduced the Atlantic Meridional Overturning Circulation (AMOC) and affected global climate[29,31]. Therefore, to evaluate ENSO changes during these abrupt events, we conducted additional CESM1.2 time slice simulations at 12 and 15 ka BP by prescribing 0.2 Sv freshwater forcings (FWFs) over the northern North Atlantic Ocean (50–70°N, 80°W–20°E) throughout the simulations. These FWF experiments are integrated over 600 years, and we analyze the last 500 years after the AMOC and tropical Pacific climate stabilize. After stabilization, AMOC strength is reduced by 40–50% relative to respective control simulations.

To compare simulated oceanic variability directly with coral $\delta^{18}O$ data, monthly SST and sea surface salinity (SSS) output from the CESM1.2 time slice simulations were forward-modelled (FM) to monthly $\delta^{18}O_{FM}$[58,59]. We further perturbed $\delta^{18}O_{FM}$ with a proxy system model (PSM) to produce monthly $\delta^{18}O_{PSM}$ that incorporates the effects of dating and analytical uncertainty[42]. Using Monte Carlo analysis, we generated 100 $\delta^{18}O_{PSM}$ realizations for each time slice simulation. Due to the westward displacement of ENSO anomaly patterns in the PI-control simulation, we used the southwest Pacific area (SWP; 16.5–14.5°S, 162.5–165.5°E) as the simulated representation for Espiritu Santo, Vanuatu (15.5°S, 167°E). The central equatorial Pacific (CEP) site (2°N, 157.5°W), the simulated representation for Kiritimati, is defined by its true grid point.

Interannual variability and ENSO amplitude

ENSO has characteristic interannual time scales of 3–8 years determined by dynamical adjustments of the equatorial ocean[67,70,71]. To separate interannual variability associated with ENSO from slow variations in the background climate, we applied a high-pass filter with a 15-year cutoff period to monthly observed SST, coral $\delta^{18}O$ records, and CESM1.2 SST, $\delta^{18}O_{FM}$, and $\delta^{18}O_{PSM}$ time slice simulations. Many previous ENSO reconstruction studies used a 9-year high-pass cutoff period[20,23,24,42], but we found a 15-year cutoff period better preserves individual ENSO event amplitude, which exhibits pronounced decadal modulation[72]. Monthly data are converted to anomalies by removing the monthly climatology, then processed with the 15-year high-pass filter, before smoothing with a 3-month running mean filter to suppress subseasonal variability. The monthly climatology is defined for the full length of each coral record and model simulation (Figs.

2–3). The analysis of observed SST and modern coral records uses a 1961–1990 CE reference period (Fig. 1).

In both the model and observations, the ENSO index is defined as high-pass filtered and smoothed SSTA averaged in the Niño 3.4 region (5°S–5°N, 170°–120°W), and we use the variance of this index as a measure of ENSO amplitude. ENSO amplitude is calculated within moving 30-year windows, stepped every 5 years, to capture the range of natural and forced variability. Multidecadal windows of interannual variance are an established metric of ENSO strength[20,23,24,42] and are necessary for evaluating forced changes in ENSO amplitude in the presence of large internal variability. Because individual ENSO events are highly stochastic and coral records are typically short (often 20–30 years in length), estimating ENSO amplitude from single events or short segments would be dominated by internal variability rather than forced changes. Using moving multidecadal windows allows us to quantify the full range of natural variability and to compare model and proxy estimates on a common statistical footing. We use 30-year windows because this length is long enough to average over several ENSO cycles (3–8-year periods) while still short enough to resolve meaningful differences among CESM1.2 time slices and among coral intervals, and it matches the minimum duration required for robust variance estimates in both paleoclimate reconstructions and climate-model analysis.

Attribution of interannual variability changes to ENSO in CESM1.2

Vanuatu is strongly influenced by ENSO during the historical period[73,74]. However, the amplitude of interannual variability at this location is affected not only by ENSO but also by multiple other factors, including regional processes and remote forcings from the extratropical South Pacific and the Indian Ocean, which may change independently of ENSO[75]. To assess past ENSO amplitude changes using coral $\delta^{18}O$ records recovered outside the Niño 3.4 region, we decomposed changes in total interannual variance into those attributable to ENSO across the tropical Pacific using $\delta^{18}O_{FM}$ from the CESM1.2 time slice simulations (Fig. 3e–h and Extended Data Fig. 1j–p). In each CESM1.2 time slice simulation, we estimated $\delta^{18}O_{FM}$ anomalies related to ENSO using a linear regression against the Niño 3.4 SST index at each model grid point as

$$\hat{y}_k = \beta_k x_k, \quad (1)$$

where $\hat{y}_k$ is the portion of $\delta^{18}O_{FM}$ anomaly y_k related to ENSO, x_k is the Niño 3.4 SST index, and β_k is the linear regression coefficient of y_k onto x_k in the time slice k. ENSO-related $\delta^{18}O_{FM}$ variance $\sigma^2_{\hat{y}_k}$ is expressed as

$$\sigma^2_{\hat{y}_k} = \beta_k^2 \sigma^2_{x_k}, \quad (2)$$

where $\sigma^2_{x_k}$ is the variance of the Niño 3.4 SST index, and its change relative to the PI-control simulation ($k = 0$) is obtained as

$$\Delta\sigma^2_{\hat{y}_k} = \beta_k^2 \sigma^2_{x_k} - \beta_0^2 \sigma^2_{x_0}. \quad (3)$$

The total interannual $\delta^{18}O_{FM}$ variance changes relative to the PI control are highly correlated with $\Delta\sigma^2_{\hat{y}_k}$ in all CESM1.2 time slice simulations (Fig. 3e–h), indicating that we can infer past ENSO changes from Vanuatu coral records. We note that Eq. (3) includes the effect of changes in both ENSO amplitude ($\sigma^2_{x_k}$) and pattern (β_k^2). Further decomposition of ENSO-related variance indicates that the amplitude effect dominates the pattern effect except near the nodal lines of the

ENSO teleconnection pattern in the PI-control simulation. Lastly, we omit all variance changes that are statistically insignificant using Kolmogorov–Smirnov testing at a 5% significance level (white regions; Fig. 3 and Extended Data Fig. 1c–p).

Extreme El Niño event analysis

Extreme El Niño events are identified using November–December–January (NDJ) Niño 3.4 SSTA. Monthly Niño 3.4 variance peaks in December in observations and in most CESM1.2 time slices except at 2xCO_2, which peaks in November, and the 12-ka and 15-ka FWF experiments, which show double peaks in February/March and June/July (Extended Data Fig. 2e,f). Because an absolute SSTA threshold cannot be directly related to coral $\delta^{18}O$ anomalies, we define extreme El Niño events in CESM1.2 using a percentile-based threshold. Specifically, the 93rd percentile of NDJ Niño 3.4 SSTA in the PI-control simulation is chosen because it yields an extreme El Niño frequency (7 events per century, by definition) that aligns with the frequency of extreme events identified using the commonly used 2 °C threshold in the modern instrumental Niño 3.4 SSTA record[76]. Using this percentile also avoids artificially inflating the number of extreme events in CESM1.2, as this model overestimates ENSO amplitude in the PI-control (Extended Data Fig. 10a) compared to historical observations. For each CESM1.2 time slice, we compute the frequency of extreme El Niño events using the 93rd percentile threshold derived from the PI-control simulation. Across all time slices, extreme El Niño events almost never occur in consecutive years. Only a single two-year sequence is detected in the CO_2-doubling future simulation, consistent with the absence of back-to-back extreme events in the observational record and with ENSO's characteristic tendency for strong El Niño events to transition into La Niña conditions.

Local extreme events are defined using site-specific percentile thresholds of NDJ simulated $\delta^{18}O_{PSM}$ and coral $\delta^{18}O$ anomalies, which reflect regional oceanic and hydroclimate conditions that can be influenced by ENSO as well as other climate processes. Positive modern/PI-control $\delta^{18}O$ anomalies above the 93rd percentile indicate local extremes in Vanuatu, whereas negative anomalies below the 7th percentile indicate local extremes at Kiritimati (i.e., in the direction of El Niño-related anomalies). For each CESM1.2 time slice and for the coral records, we compute the frequency of local extreme events using these site-specific thresholds (Supplementary Table 6).

To align coral data with CESM1.2 time slices, we grouped individual coral records into their corresponding age intervals. For example, Vanuatu coral $\delta^{18}O$ records younger than 1.5 ka were assigned to the 1.5–0-ka interval and compared to the PI-control time slice, whereas Kiritimati corals dated to 7.5–4.5 ka were assigned to that interval and compared to the 6-ka time slice. Partial-year coral segments were removed from each record, and only full-year segments were retained for analysis. Within each interval, interannual variance and extreme-event frequency were calculated for each record independently and then combined using length-weighted means to obtain interval-level estimates. To minimize aliasing, only records at least 20 years in length were included. The resulting effective interval lengths (Fig. 4b,c, parenthesized values) reflect the total usable years contributing to each weighted estimate.

Local extreme El Niño-coeval events are defined as local $\delta^{18}O$ extremes that occur in the same NDJ season as an extreme El Niño event in CESM1.2. Identifying these coeval events allows us to evaluate the extent to which local extreme events coincide with extreme El Niño conditions, and to assess whether changes in local extremes through time parallel changes in Niño 3.4 extremes. Because both the $\delta^{18}O_{FM}$ and $\delta^{18}O_{PSM}$ series incorporate chronological uncertainty arising from age-model construction, we additionally allow a ±1-year lead/lag window when pairing local extremes with Niño 3.4 extremes. This window accommodates the realistic age uncertainty in the local simulations and prevents misclassification of events that are effectively synchronous but offset by small age-model errors. Using this approach, we calculate the fraction of coeval extreme events in $\delta^{18}O_{FM}$ and $\delta^{18}O_{PSM}$ at SWP and CEP for each CESM1.2 time slice. This dual perspective of assessing non-coeval and coeval local extremes provides a basis for evaluating the relationship between El Niño extremes and local oceanic and hydroclimate extremes during intervals with overlapping model and coral coverage, and for interpreting synchronous local extreme El Niño-coeval events in intervals lacking direct Niño 3.4 constraints.

Extended Data Fig. 1: Simulated tropical Pacific interannual and ENSO-explained variance changes and coral coverage since the last deglaciation.

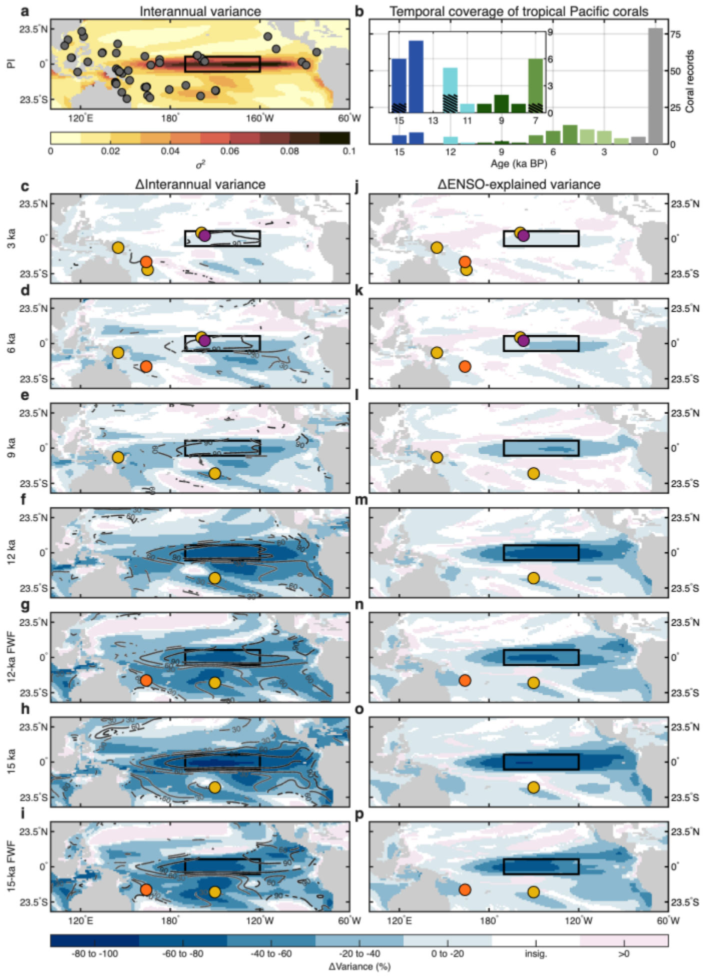

a, Interannual $\delta^{18}O_{FM}$ anomaly variance at the PI control. Grey circles depict locations of subannually resolved coral records dated to 1.5 ka and younger. **b**, Temporal coverage of subannually resolved tropical Pacific coral records (Supplementary Table 1), grouped by number of records in each interval. Hatching in inset depicts this study's coral contribution. **c**–**i**, Changes in interannual $\delta^{18}O_{FM}$ anomaly variance from 3 ka to 15-ka FWF, respectively. Grey contours depict the ENSO-explained variance change as a percentage of the interannual variance change where both are significant (Methods). **j**–**p**, Changes in ENSO-explained $\delta^{18}O_{FM}$ anomaly variance from 3 ka to 15-ka FWF, respectively. In **c**–**p**), white regions are where changes are statistically insignificant (Methods). Colored circles depict sites – Vanuatu (orange), Kiritimati (purple) and other locations (gold) – where there are subannually resolved coral records dated to within 1,500 years of both the modern era and each time slice. Percent changes other than contours are relative to the PI control. Black box depicts the Niño 3.4 region.

Extended Data Fig. 2: Changes in the seasonal cycle and variability of Niño 3.4 SST across CESM1.2 freshwater forcing experiments.

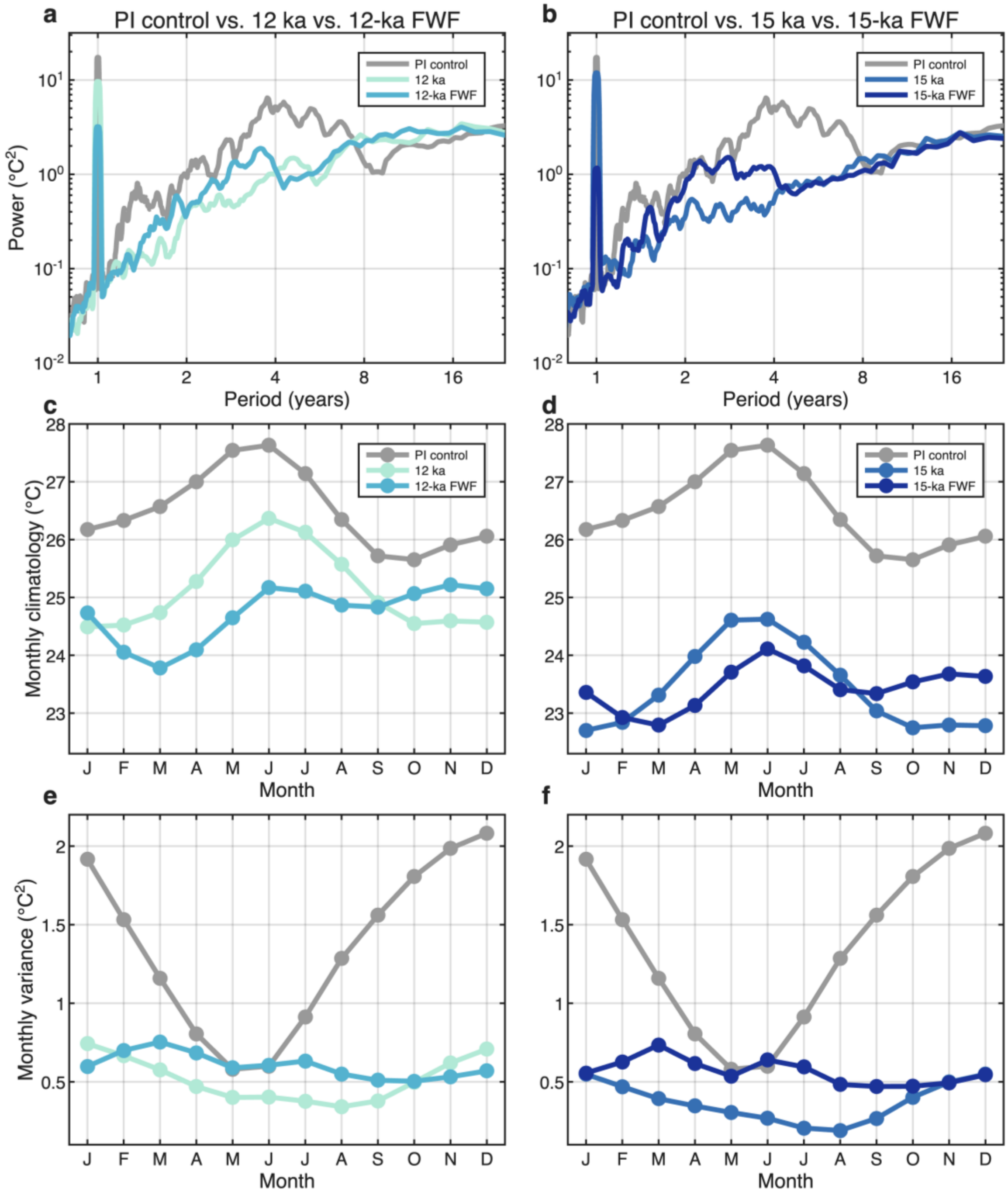

a,**b**, Power spectra, **c**,**d**, monthly climatology, and **e**,**f**, variance of Niño 3.4 SST compared between the standard and freshwater forcing (FWF) time slices at 12 ka (**a**,**c**,**e**) and 15 ka (**b**,**d**,**f**) (colored contours), as well as the PI control (gray contours). Legend in **c**) also applies to **e**), and legend in **d**) also applies to **f**.

740 **Extended Data Fig. 3: Vanuatu coral collection sites.**

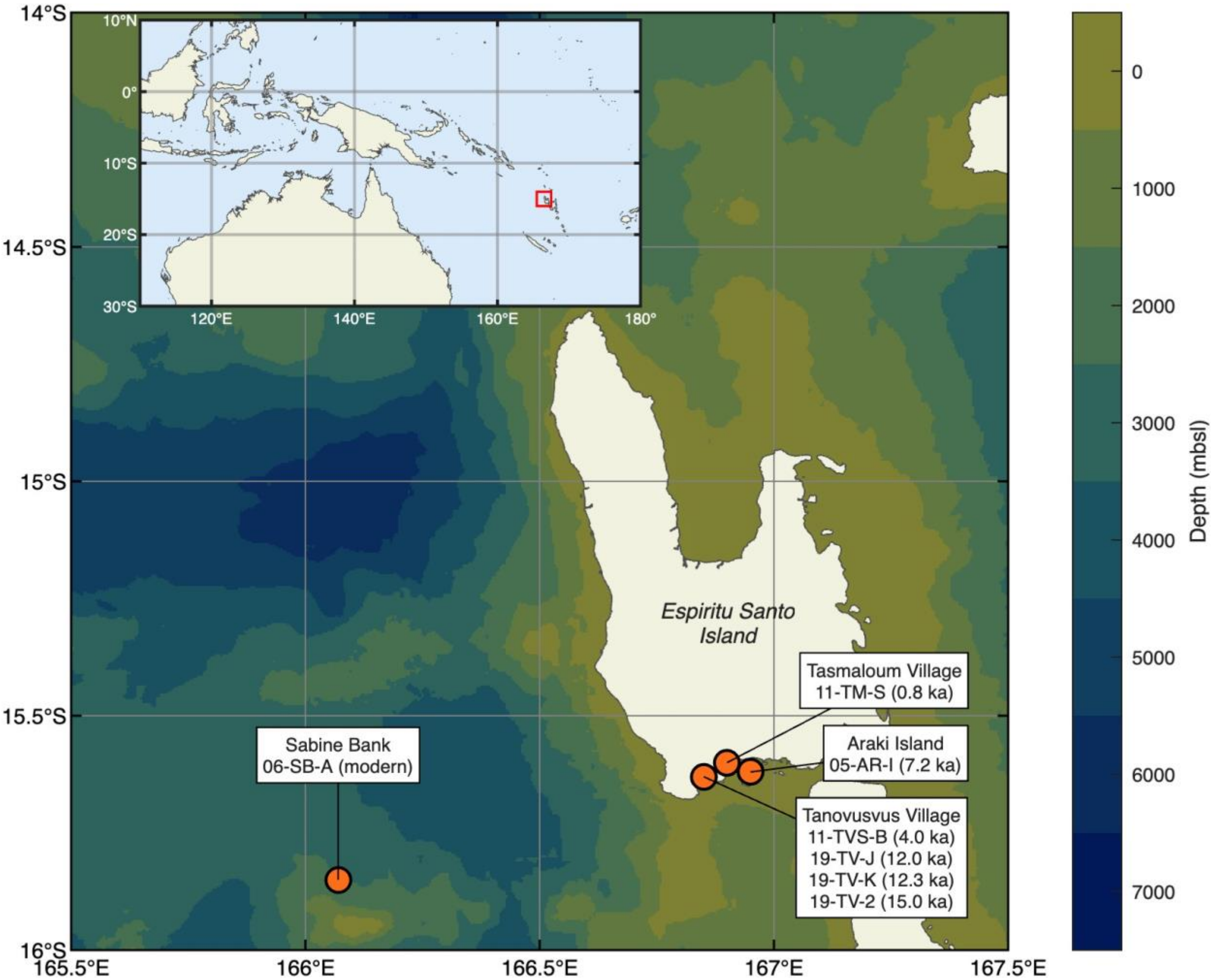

Coral samples collected at each site are listed with approximate ages in parentheses. 06-SB-A and 11-TM-S are previously published. Bathymetry is from the GEBCO 2025 Grid[77,78].

Extended Data Fig. 4: Vanuatu coral 11-TVS-B.

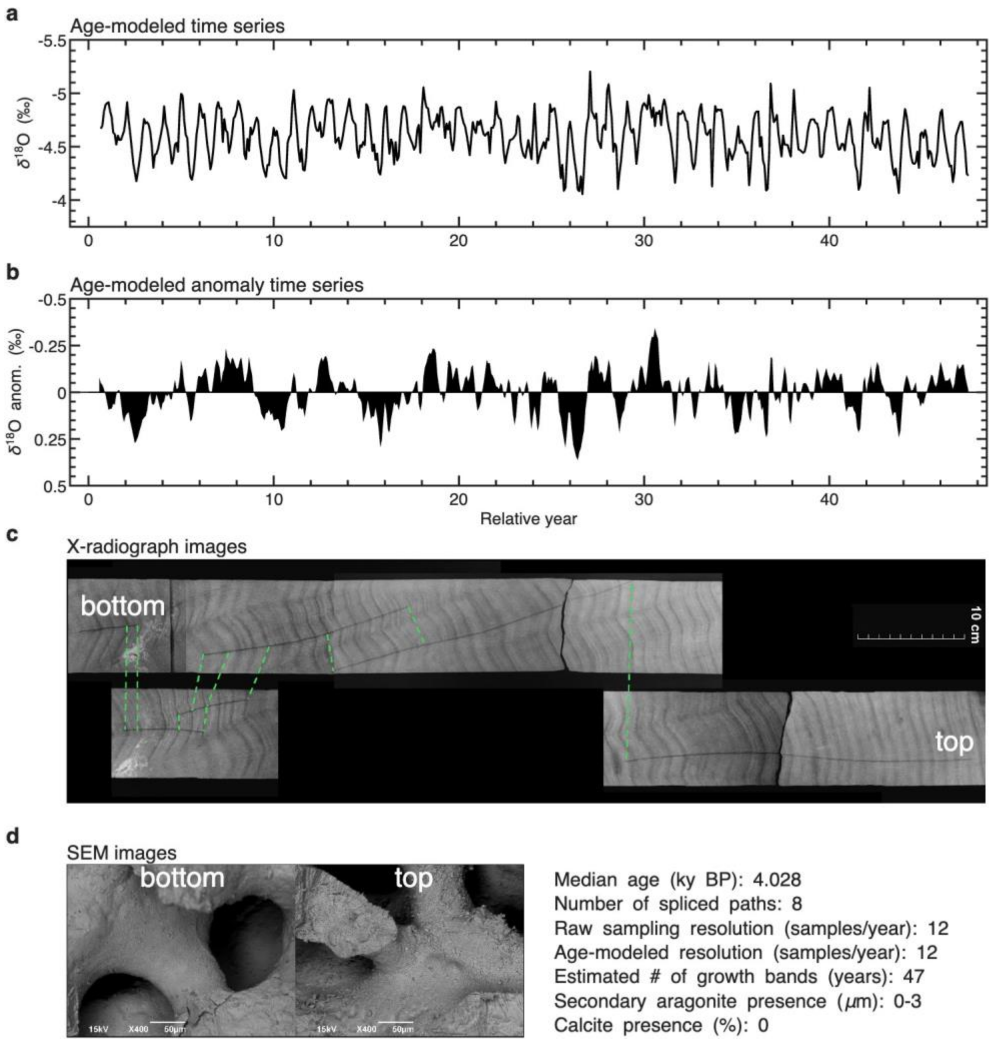

a, Composite $\delta^{18}O$ time series of 11-TVS-B, collected in 2011 at the coastline near Tanovusvus Village, Espiritu Santo Island, Vanuatu, and processed with an age-model algorithm[42]. **b**, Monthly anomalies of the age-modelled $\delta^{18}O$ time series. **c**, Composite x-radiograph images of sampled paths with overlapping portions marked by green dashes. The rightmost path is not included in the time series in **a**) and **b**). **d**, SEM images of the coral specimen. In **a**) and **b**), the y-axes are flipped to show the reverse relationship to SST. Time moves to the right. Age, sampling, and diagenetic metrics are provided.

Extended Data Fig. 5: Vanuatu coral 05-AR-I.

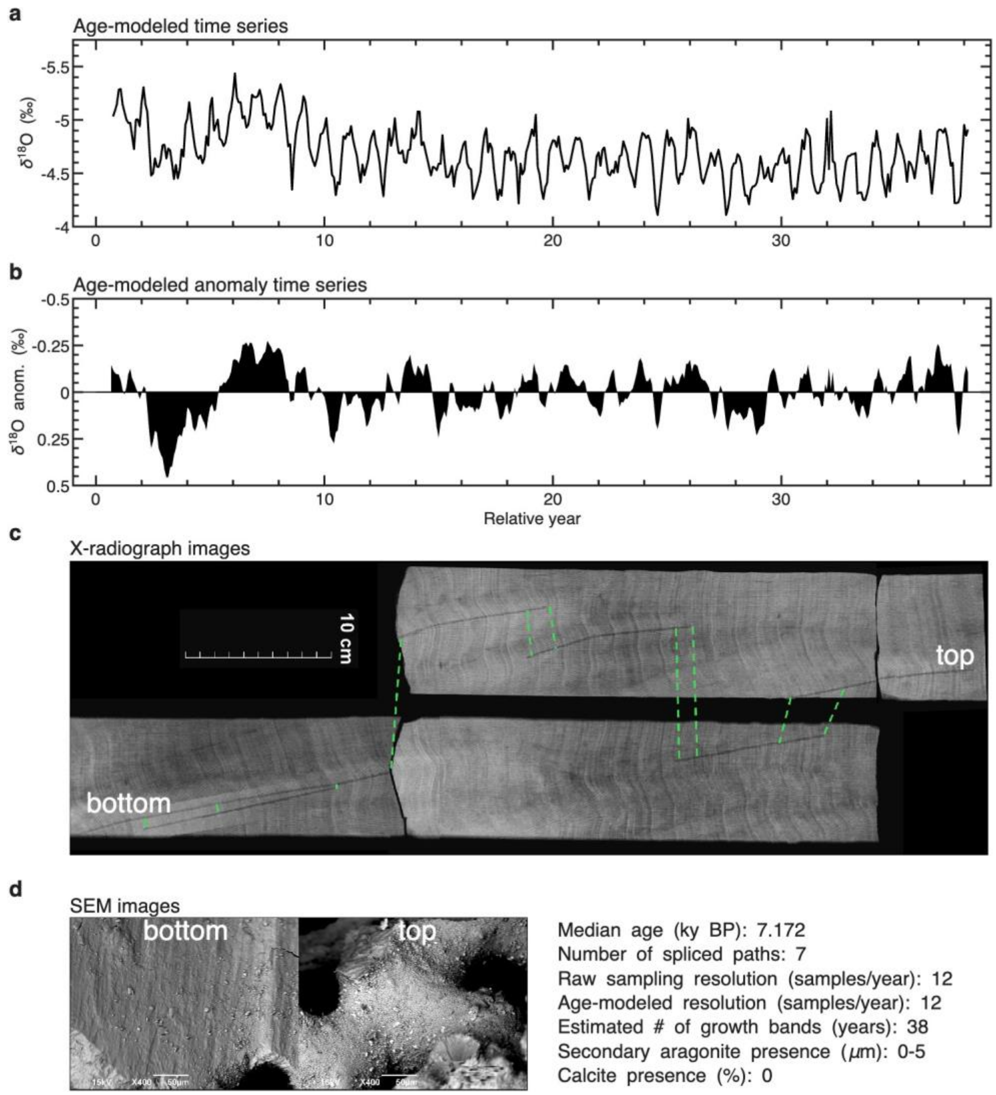

a, Composite $\delta^{18}O$ time series of 05-AR-I, collected in 2005 at the coastline of Araki Island, Vanuatu, and processed with an age-model algorithm[42]. **b**, Monthly anomalies of the age-modelled $\delta^{18}O$ time series. **c**, Composite x-radiograph images of sampled paths with overlapping portions marked by green dashes. **d**, SEM images of the coral specimen. In **a**) and **b**), the y-axes are flipped to show the reverse relationship to SST. Time moves to the right. Age, sampling, and diagenetic metrics are provided.

Extended Data Fig. 6: Vanuatu coral 19-TV-J.

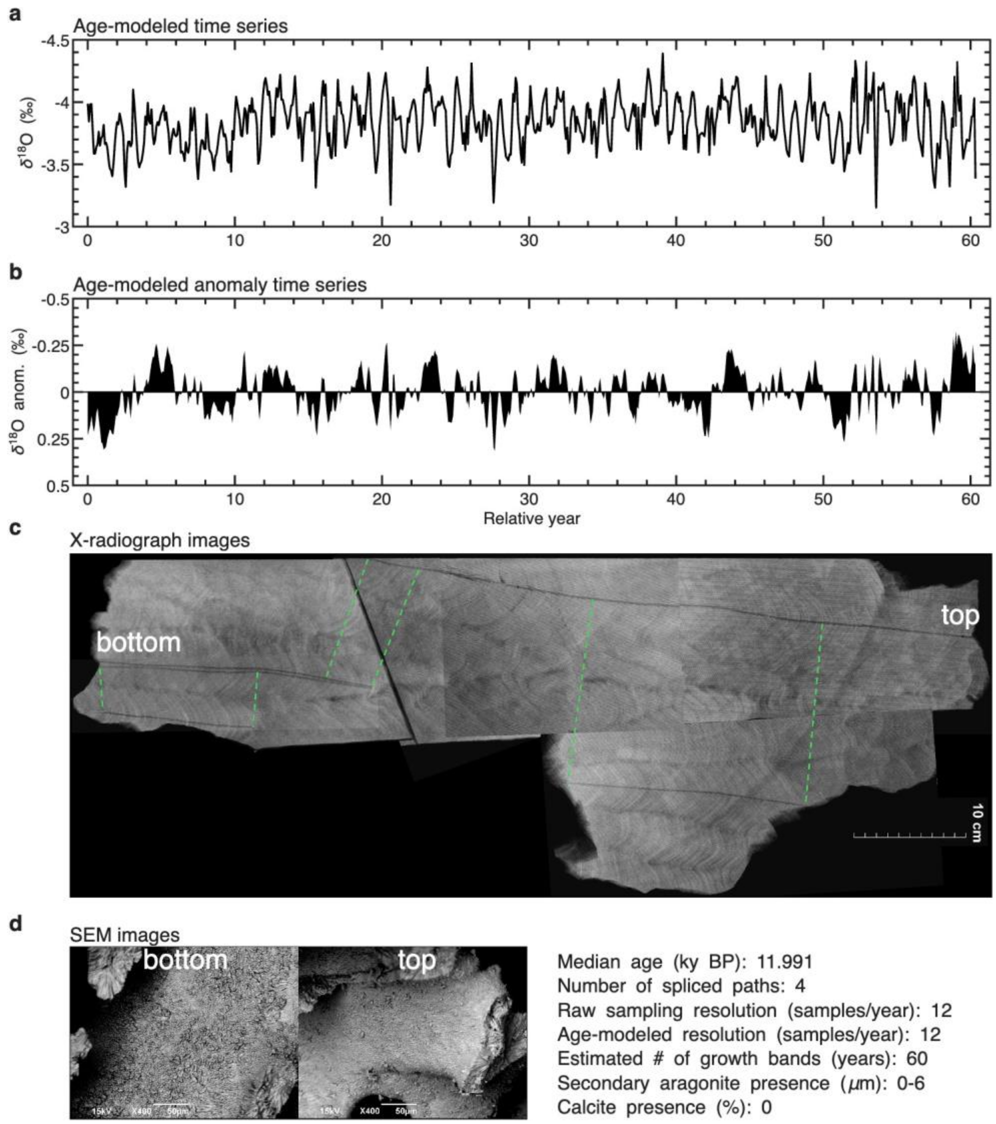

a, Composite $\delta^{18}O$ time series of 19-TVS-J, collected in 2019 at the coastline near Tanovusvus Village, Espiritu Santo Island, Vanuatu, and processed with an age-model algorithm[42]. **b**, Monthly anomalies of the age-modelled $\delta^{18}O$ time series. **c**, Composite x-radiograph images of sampled paths with overlapping portions marked by green dashes. The path directly below the 'bottom' text is not included in the time series in **a**) and **b**). **d**, SEM images of the coral specimen. In **a**) and **b**), the y-axes are flipped to show the reverse relationship to SST. Time moves to the right. Age, sampling, and diagenetic metrics are provided.

Extended Data Fig. 7: Vanuatu coral 19-TV-K.

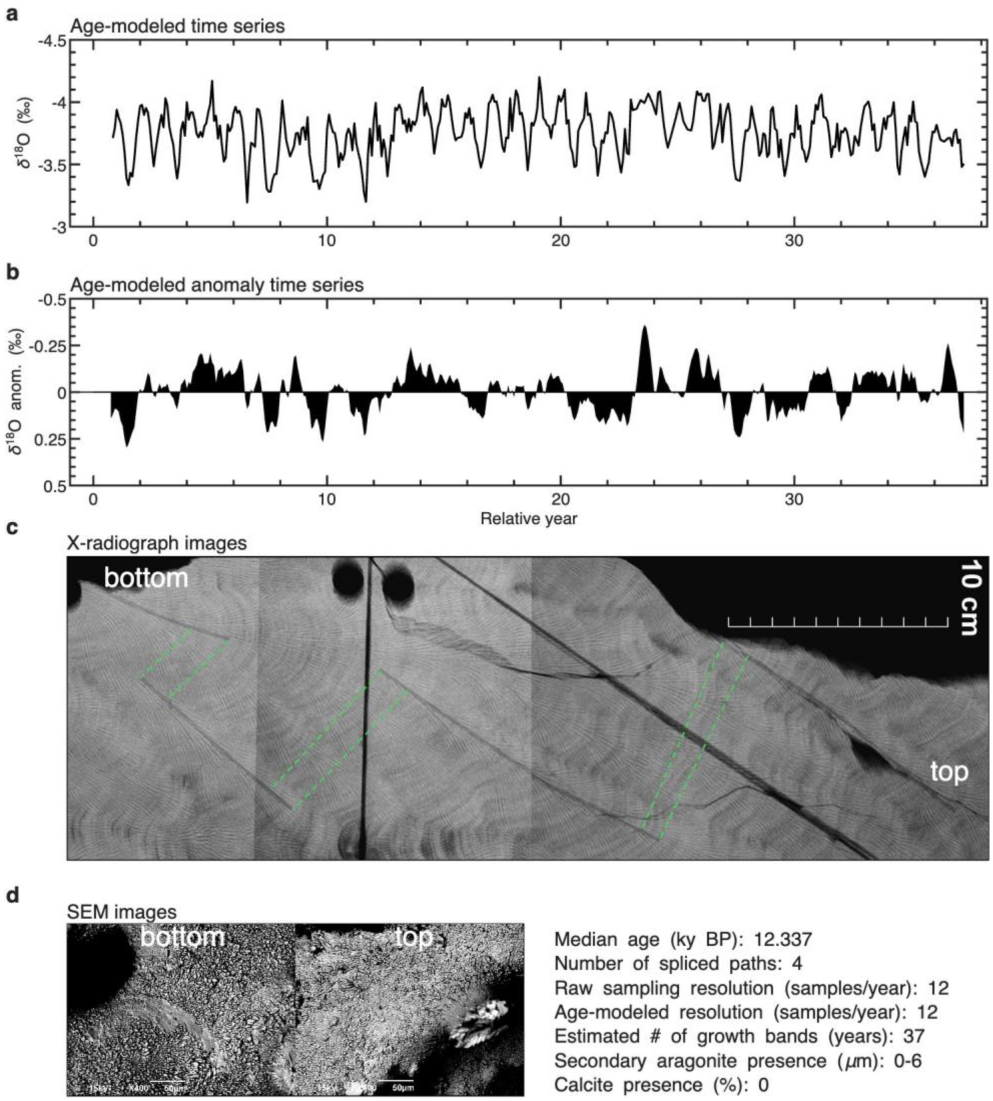

a, Composite $\delta^{18}O$ time series of 19-TVS-K, collected in 2019 at the coastline near Tanovusvus Village, Espiritu Santo Island, Vanuatu, and processed with an age-model algorithm[42]. **b**, Monthly anomalies of the age-modelled $\delta^{18}O$ time series. **c**, Composite x-radiograph images of sampled paths with overlapping portions marked by green dashes. In **a**) and **b**), the y-axes are flipped to show the reverse relationship to SST. Time moves to the right. Age, sampling, and diagenetic metrics are provided.

Extended Data Fig. 8: Vanuatu coral 19-TV-2.

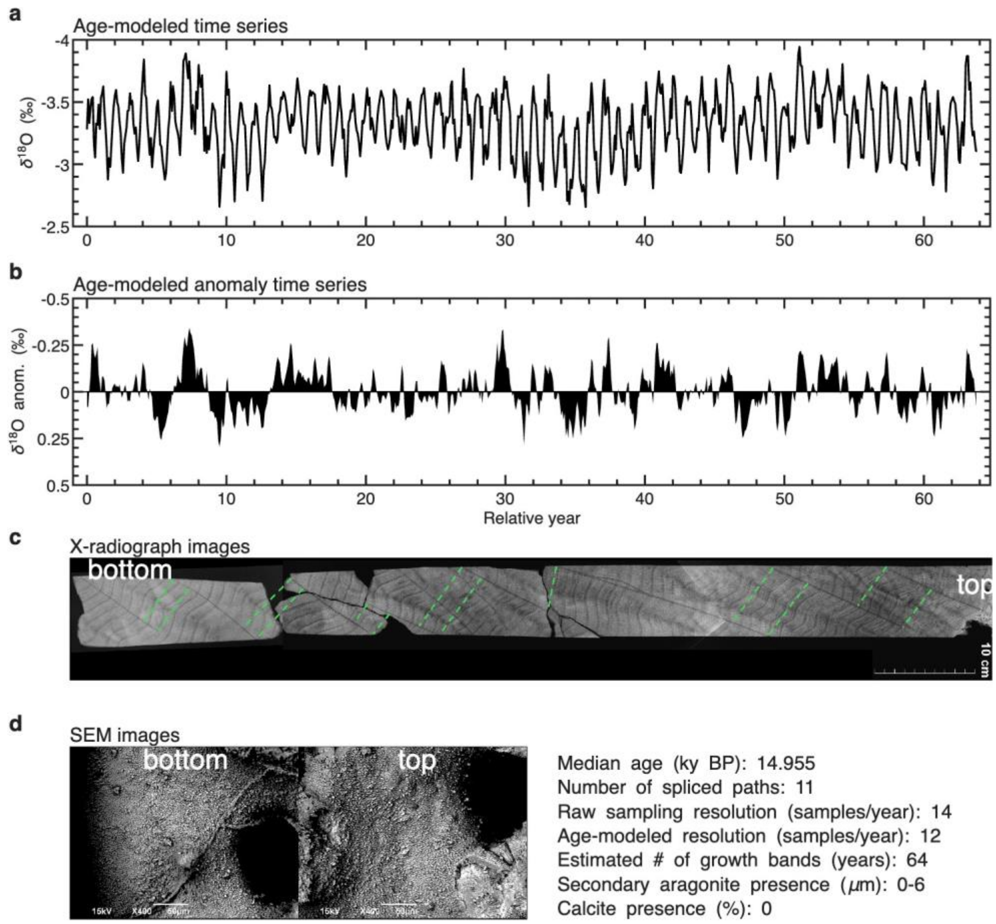

a, Composite $\delta^{18}O$ time series of 19-TV-2, collected in 2019 at the coastline near Tanovusvus Village, Espiritu Santo Island, Vanuatu, and processed with an age-model algorithm[42]. **b**, Monthly anomalies of the age-modelled $\delta^{18}O$ time series. **c**, Composite x-radiograph images of sampled paths with overlapping portions marked by green dashes. **d**, SEM images of the coral specimen. In **a**) and **b**), the y-axes are flipped to show the reverse relationship to SST. Time moves to the right. Age, sampling, and diagenetic metrics are provided.

Extended Data Fig. 9: Observed annual cycle and modern coral records at Kiritimati.

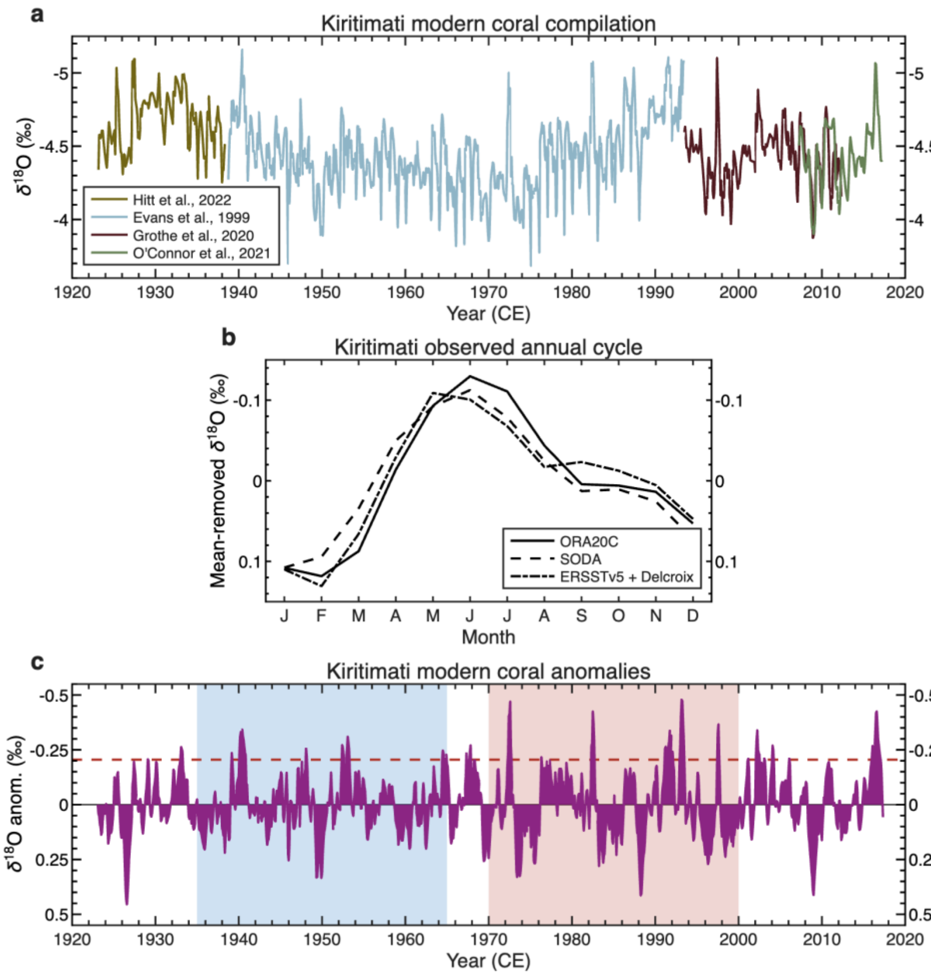

a, A composite monthly $\delta^{18}O$ time series of the modern Kiritimati coral compilation (1923–2017 CE). Each record is processed with an age-model algorithm to appropriately compare modern and fossil corals (Methods). Missing data (1929–1930 CE) in the Hitt et al.[79] (2022) record was replaced with the Evans et al.[80] (1999) annual cycle for record continuity. A 0.027‰ offset was subtracted from the Grothe et al.[23] (2020) record, and a 0.405‰ offset was added to the O'Connor et al.[81] (2021) record. **b**, The mean-removed $\delta^{18}O$ annual cycle at Kiritimati, forward-modelled from monthly SST and sea surface salinity (SSS) from the ORA-20C (1900–2009 CE) and SODA (1871–2010 CE) ocean reanalysis products, and from ERSSTv5 SST combined with the Delcroix et al.[57] (2011) SSS ocean reanalysis dataset (1950–2009 CE). **c**, Monthly $\delta^{18}O$ anomalies from the Kiritimati modern coral compilation. Shaded intervals in represent historically weaker (blue, 1935–1964 CE) and stronger (pink, 1970–1999 CE) ENSO periods. The dashed red line depicts the extreme El Niño threshold at the 7th percentile of November–December–January averaged (NDJ) coral $\delta^{18}O$ anomalies. All y-axes are flipped to show the reverse relationship to SST.

Extended Data Fig. 10: Simulated extreme El Niño frequency across changes in ENSO strength.

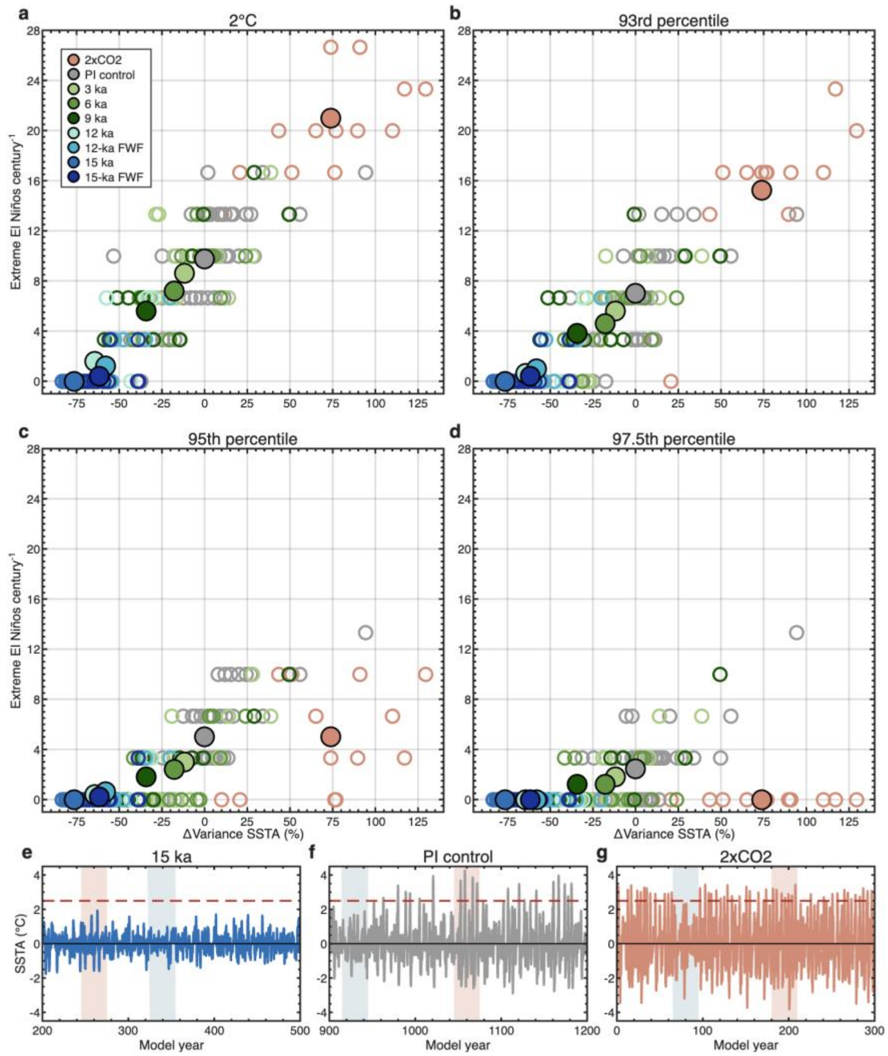

a–**d**, Relationship between Niño 3.4 ENSO variance and extreme El Niño frequency (Methods) in CESM1.2 since the last deglaciation and at an atmospheric CO_2 doubling (2xCO2), where the extreme El Niño threshold is defined as 2°C (**a**), the 93rd percentile (**b**), the 95th percentile (**c**), and the 97.5th percentile (**d**) of the NDJ average of the PI-control simulation. Filled symbols represent full-simulation variances, and open symbols represent 30-year non-overlapping variances. **e**–**g**, Simulated monthly Niño 3.4 SSTA time series in selected 300-year intervals forced by background conditions at 15 ka (**e**), the PI control (**f**), and 2xCO2 (**g**). Dashed red lines are the 93rd percentile of the NDJ average SSTA in the PI control, defining the extreme El Niño threshold (2.5°C) for simulated Niño 3.4 SSTA. Light blue (pink) shaded areas depict 30-year windows of weaker (stronger) ENSO due to internal variability.

References (for Manuscript, Figures, Methods, & Extended Data Figures)

1. Cai, W. *et al.* Increasing frequency of extreme El Niño events due to greenhouse warming. *Nature Climate Change* **4**, 111–116 (2014).
2. Wang, B. *et al.* Historical change of El Niño properties sheds light on future changes of extreme El Niño. *Proc Natl Acad Sci U S A* **116**, 22512–22517 (2019).
3. Brown, J. R. *et al.* Comparison of past and future simulations of ENSO in CMIP5/PMIP3 and CMIP6/PMIP4 models. *Climate of the Past* **16**, 1777–1805 (2020).
4. Cai, W. *et al.* ENSO Response to Greenhouse Forcing. in *Geophysical Monograph Series: El Niño Southern Oscillation in a Changing Climate* 289–307 (Wiley, 2020).
5. Maher, N., Matei, D., Milinski, S. & Marotzke, J. ENSO Change in Climate Projections: Forced Response or Internal Variability?. *Geophysical Research Letters* **45**, 86 (2018).
6. Holbrook, N. J. *et al.* A global assessment of marine heatwaves and their drivers. *Nature Communications* **10**, 2624 (2019).
7. DeLong, K. L., Quinn, T. M., Taylor, F. W., Lin, K. & Shen, C.-C. Sea surface temperature variability in the southwest tropical Pacific since AD 1649. *Nature Climate Change* **2**, 799–804 (2012).
8. Beobide-Arsuaga, G., Bayr, T., Reintges, A. & Latif, M. Uncertainty of ENSO-amplitude projections in CMIP5 and CMIP6 models. *Climate Dynamics* **56**, 3875–3888 (2021).
9. Fredriksen, H., Berner, J., Subramanian, A. C. & Capotondi, A. How Does El Niño–Southern Oscillation Change Under Global Warming—A First Look at CMIP6. *Geophysical Research Letters* **47**, 123 (2020).
10. Heede, U. K. & Fedorov, A. V. Towards understanding the robust strengthening of ENSO and more frequent extreme El Niño events in CMIP6 global warming simulations. *Climate Dynamics* **61**, 3047–3060 (2023).

11. IPCC. *Climate Change 2023: Synthesis Report. Contribution of Working Groups I, II and III to the Sixth Assessment Report of the Intergovernmental Panel on Climate Change* (Intergovernmental Panel on Climate Change (IPCC), 2023).

12. Zhu, J. *et al.* Reduced ENSO variability at the LGM revealed by an isotope-enabled Earth system model. *Geophysical Research Letters* **44**, 6984–6992 (2017).

13. Han, T., de Winter, N. J., Liu, C., Zhao, N. & Yan, H. Quantifying Past ENSO Variability From Tridacna δ18O Using a Pseudo-Proxy Baseline Approach. *Paleoceanography and Paleoclimatology* **41**, 0 (2026).

14. Huang, J. *et al.* Persistent El Niño-like conditions over the western Pacific during the Bølling–Allerød interstadial. *Communications Earth & Environment* **7**, 0 (2025).

15. Lu, W. *et al.* Warmer shallow Atlantic during deglaciation and early Holocene due to weaker overturning circulation. *Nature Geoscience* **18**, 787–792 (2025).

16. Yseki, M. *et al.* El Niño–Southern Oscillation strengthened by North Atlantic Iceberg discharge during Heinrich stadial 1. *Communications Earth & Environment* **7**, 0 (2026).

17. Pontes, G. M., da Silva Dias, P. L. & Menviel, L. Rapid communication: Nonlinear sensitivity of the El Niño–Southern Oscillation across climate states. *Climate of the Past* **21**, 1079–1091 (2025).

18. Tiwari, S. *et al.* Mid-Holocene El Niño Southern Oscillation variability reduced by northern African vegetation changes in climate models. *Communications Earth & Environment* **6**, 0 (2025).

19. Wittenberg, A. T., Rosati, A., Delworth, T. L., Vecchi, G. A. & Zeng, F. ENSO Modulation: Is It Decadally Predictable?. *Journal of Climate* **27**, 2667–2681 (2014).

20. Lawman, A. E. *et al.* Unraveling forced responses of extreme El Niño variability over the Holocene. *Science Advances* **8**, eabm4313 (2022).

21. Thirumalai, K. *et al.* Future increase in extreme El Niño supported by past glacial changes. *Nature* **634**, 374–380 (2024).

22. Cobb, K. M. *et al.* Highly Variable El Niño–Southern Oscillation Throughout the Holocene. *Science* **339**, 67–70 (2013).

23. Grothe, P. R. *et al.* Enhanced El Niño–Southern Oscillation Variability in Recent Decades. *Geophysical Research Letters* **47**, e2019GL083906 (2020).

24. Lawman, A. E. *et al.* A century of reduced ENSO variability during the Medieval Climate Anomaly. *Paleoceanography and Paleoclimatology* **35**, e2019PA003742 (2020).

25. McGregor, H. V. *et al.* A weak El Niño/Southern Oscillation with delayed seasonal growth around 4,300 years ago. *Nature Geoscience* **6**, 949–953 (2013).

26. Corrège, T. *et al.* Interdecadal variation in the extent of South Pacific tropical waters during the Younger Dryas event. *Nature* **428**, 927–929 (2004).

27. Taylor, F. W., Edward, R. L., Wasserburg, G. J. & Frohlich, C. Seismic recurrence intervals and timing of aseismic subduction inferred from emerged corals and reefs of the central Vanuatu (New Hebrides) frontal arc. *Journal of Geophysical Research: Solid Earth* 393–408 (1990).

28. Voosen, P. The coral chronicles. *Science* **383**, 472–477 (2024).

29. Alley, R. B. The Younger Dryas cold interval as viewed from central Greenland. *Quaternary Science Reviews* **19**, 213–226 (2000).

30. Denton, G. H. *et al.* The Last Glacial Termination. *Science* **328**, 1652–1656 (2010).

31. McManus, J. F., Francois, R., Gherardi, J. M., Keigwin, L. D. & Brown-Leger, S. Collapse and rapid resumption of Atlantic meridional circulation linked to deglacial climate changes. *Nature* **428**, 834–837 (2004).

32. Liu, W., Pinto, D. D. C., Fedorov, A. & Zhu, J. The Impacts of a Weakened Atlantic Meridional Overturning Circulation on ENSO in a Warmer Climate. *Geophysical Research Letters* **50**, e2023GL103025 (2023).

33. Merkel, U., Prange, M. & Schulz, M. ENSO variability and teleconnections during glacial climates. *Quaternary Science Reviews* **29**, 86–100 (2010).

34. Orihuela-Pinto, B., England, M. H. & Taschetto, A. S. Interbasin and interhemispheric impacts of a collapsed Atlantic Overturning Circulation. *Nature Climate Change* **12**, 558–565 (2022).

35. Timmermann, A. *et al.* The Influence of a Weakening of the Atlantic Meridional Overturning Circulation on ENSO. *Journal of Climate* **20**, 4899–4919 (2007).

36. Williamson, M. S. *et al.* Effect of AMOC collapse on ENSO in a high resolution general circulation model. *Climate Dynamics* **50**, 2537–2552 (2018).

37. Yang, Y. *et al.* Weakened Atlantic Meridional Overturning Circulation Contributes to Opposite Responses of ENSO and the Atlantic Niño/Niña to Greenhouse Warming. *Geophysical Research Letters* **52**, 1 (2025).

38. Zhang, R. & Delworth, T. L. Simulated Tropical Response to a Substantial Weakening of the Atlantic Thermohaline Circulation. *Journal of Climate* **18**, 1853–1860 (2005).

39. Zhang, R. *et al.* A Review of the Role of the Atlantic Meridional Overturning Circulation in Atlantic Multidecadal Variability and Associated Climate Impacts. *Reviews of Geophysics* **57**, 316–375 (2019).

40. Xie, S.-P., Okumura, Y., Miyama, T. & Timmermann, A. Influences of Atlantic climate change on the tropical Pacific via the Central American Isthmus. *Journal of Climate* **21**, 3914–3928 (2008).

41. Glaubke, R. H. *et al.* An Inconsistent ENSO Response to Northern Hemisphere Stadials Over the Last Deglaciation. *Geophysical Research Letters* **51**, 1 (2024).

42. Lawman, A. E. *et al.* Developing a coral proxy system model to compare coral and climate model estimates of changes in paleo-ENSO variability. *Paleoceanography and Paleoclimatology* **35**, e2019PA003836 (2020).

43. Shakun, J. D. *et al.* Global warming preceded by increasing carbon dioxide concentrations during the last deglaciation. *Nature* **484**, 49–54 (2012).

44. Yeh, S. *et al.* ENSO Atmospheric Teleconnections and Their Response to Greenhouse Gas Forcing. *Reviews of Geophysics* **56**, 185–206 (2018).

45. Tindall, J. C., Haywood, A. M. & Thirumalai, K. Modeling the stable water isotope expression of El Niño in the Pliocene: Implications for the interpretation of proxy data. *Paleoceanography* **32**, 881–902 (2017).

46. Power, S., Delage, F., Chung, C., Kociuba, G. & Keay, K. Robust twenty-first-century projections of El Niño and related precipitation variability. *Nature* **502**, 541–545 (2013).

47. Xing, Q. *et al.* Meridionally consistent decline in the observed western boundary contribution to the Atlantic Meridional Overturning Circulation. *Science Advances* **12**, eadz7738 (2026).

48. Bellomo, K., Angeloni, M., Corti, S. & von Hardenberg, J. Future climate change shaped by inter-model differences in Atlantic meridional overturning circulation response. *Nature Communincations* **12**, 3659 (2021).

49. Spratt, R. M. & Lisiecki, L. E. A Late Pleistocene sea level stack. *Climate of the Past* **12**, 1079–1092 (2016).

50. Shen, C.-C. *et al.* Uranium and thorium isotopic and concentration measurements by magnetic sector inductively coupled plasma mass spectrometry. *Chemical Geology* **185**, 165–178 (2002).

51. Shen, C.-C. *et al.* High-precision and high-resolution carbonate 230Th dating by MC-ICP-MS with SEM protocols. *Geochimica et Cosmochimica Acta* **99**, 71–86 (2012).

52. Hu, H.-M. *et al.* Sub-epsilon natural $^{234}U/^{238}U$ measurements refine the ^{234}U half-life and U-Th geochronology. *Science Advances* **11**, eadu8117 (2025).

53. Cheng, H. *et al.* Improvements in 230Th dating, 230Th and 234U half-life values, and U–Th isotopic measurements by multi-collector inductively coupled plasma mass spectrometry. *Earth and Planetary Science Letters* **371-372**, 82–91 (2013).

54. de Boisséson, E., Balmaseda, M. A. & Mayer, M. Ocean heat content variability in an ensemble of twentieth century ocean reanalyses. *Climate Dynamics* **50**, 3783–3798 (2018).

55. Villarroya, S., Viqueira, J. R. R., Regueiro, M. A., Taboada, J. A. & Cotos, J. M. SODA: A framework for spatial observation data analysis. *Distributed and Parallel Databases* **34**, 65–99 (2016).

56. Huang, B. *et al.* Extended Reconstructed Sea Surface Temperature, Version 5 (ERSSTv5): Upgrades, Validations, and Intercomparisons. *Journal of Climate* **30**, 8179–8205 (2017).

57. Delcroix, T., Alory, G., Cravatte, S., Corrège, T. & McPhaden, M. J. A gridded sea surface salinity data set for the tropical Pacific with sample applications (1950–2008). *Deep Sea Research Part I: Oceanographic Research Papers* **58**, 38–48 (2011).

58. LeGrande, A. N. & Schmidt, G. A. Global gridded data set of the oxygen isotopic composition in seawater. *Geophysical Research Letters* **33**, L12604 (2006).

59. Thompson, D. M., Ault, T. R., Evans, M. N., Cole, J. E. & Emile-Geay, J. Comparison of observed and simulated tropical climate trends using a forward model of coralδ18O. *Geophysical Research Letters* **38**, L14706 (2011).

60. Schneider, D. P., Deser, C., Fasullo, J. & Trenberth, K. E. Climate Data Guide Spurs Discovery and Understanding. *Eos, Transactions American Geophysical Union* **94**, 121–132 (2013).

61. Ishii, M., Shouji, A., Sugimoto, S. & Matsumoto, T. Objective analyses of sea-surface temperature and marine meteorological variables for the 20th century using ICOADS and the Kobe Collection. *International Journal of Climatology* **25**, 865–879 (2005).

62. Morice, C. P., Kennedy, J. J., Rayner, N. A. & Jones, P. D. Quantifying uncertainties in global and regional temperature change using an ensemble of observational estimates: The HadCRUT4 data set. *Journal of Geophysical Research: Atmospheres* **117**, 1203 (2012).

63. Vaccaro, A. *et al.* Climate Field Completion via Markov Random Fields: Application to the HadCRUT4.6 Temperature Dataset. *Journal of Climate* **34**, 4169–4188 (2021).

64. Morice, C. P. *et al.* An Updated Assessment of Near-Surface Temperature Change From 1850: The HadCRUT5 Data Set. *Journal of Geophysical Research: Atmospheres* **126**, 367 (2021).

65. Rayner, N. A. Global analyses of sea surface temperature, sea ice, and night marine air temperature since the late nineteenth century. *Journal of Geophysical Research* **108**, 4407 (2003).

66. Kaplan, A. *et al.* Analyses of global sea surface temperature 1856–1991. *Journal of Geophysical Research: Oceans* **103**, 18567–18589 (1998).

67. Capotondi, A., Wittenberg, A. T., Kug, J., Takahashi, K. & McPhaden, M. J. ENSO Diversity. in *Geophysical Monograph Series: El Niño Southern Oscillation in a Changing Climate* 65–86 (Wiley, 2020).

68. Okumura, Y. M. & Deser, C. Asymmetry in the Duration of El Niño and La Niña. *Journal of Climate* **23**, 5826–5843 (2010).

69. Planton, Y. Y. *et al.* Evaluating Climate Models with the CLIVAR 2020 ENSO Metrics Package. *Bulletin of the American Meteorological Society* **102**, E193–E217 (2021).

70. Timmermann, A. *et al.* El Niño-Southern Oscillation complexity. *Nature* **559**, 535–545 (2018).

71. Trenberth, K. E. ENSO in the Global Climate System. in *Geophysical Monograph Series: El Niño Southern Oscillation in a Changing Climate* 21–37 (Wiley, 2020).

72. Wittenberg, A. T. Are historical records sufficient to constrain ENSO simulations. *Geophysical Research Letters* **36**, L12702 (2009).

73. Philander, S. G. H. El Nino southern oscillation phenomena. *Nature* **302**, 295–301 (1983).

74. Tigona, R. S. & de Freitas, C. R. Relationship between the Southern Oscillation and rainfall in Vanuatu. *Weather and Climate* **32, No. 1**, 43–50 (2012).

75. DiNezio, P. N. *et al.* Climate Response of the Equatorial Pacific to Global Warming. *Journal of Climate* **22**, 4873–4892 (2009).

76. NOAA Climate Prediction Center. Oceanic Niño Index (ONI): Historical El Niño/La Niña episodes (1950–present). National Oceanic and Atmospheric Administration. https://www.cpc.ncep.noaa.gov/products/analysis_monitoring/ensostuff/ONI_v5.php. (2026).

77. GEBCO Compilation Group. GEBCO 2025 Grid. British Oceanographic Data Centre (2025).

78. Wessel, P & Smith, W. H. F. A global, self-consistent, hierarchical, high-resolution shoreline database. National Geophysical Data Center (1996).

79. Hitt, N. T. *et al.* Central Equatorial Pacific Warming and Freshening in the Twentieth Century: Insights From a Coral Ensemble Approach. *Geophysical Research Letters* **49**, e2021GL094051 (2022).

80. Evans, M. N., Fairbanks, R. G. & Rubenstone, J. L. The thermal oceanographic signal of El Niño reconstructed from a Kiritimati Island coral. *Journal of Geophysical Research: Oceans* **104**, 13409–13421 (1999).

81. O’Connor, G. K. *et al.* Coral Oxygen Isotopic Records Capture the 2015/2016 El Niño Event in the Central Equatorial Pacific. *Geophysical Research Letters* **48**, e2021GL094036 (2021).

Mandatory statements

Acknowledgments

We thank Chief Kalman Mele of the village of Tanovusvus, Edwin Tae, and the government of the Republic of Vanuatu for research access, hospitality, and accommodations, the Texas Advanced Computing Center at UT Austin for providing computing resources for model simulations on Lonestar6, Eddie Wheeler of Tech2000 in Georgetown, Texas, for building the land-based drill rig, Brandon Minton at UT Austin for his assistance collecting specimens in Vanuatu, the teams at the Paleo^2 Lab at the University of Arizona and the Stable Isotope Geosciences Facility at Texas A&M University for providing geochemical analyses, and Kenneth Befus at UT Austin for the use of XRD and SEM equipment for diagenetic analyses. We also thank Eleanor Cote and Bradley Ibarra at UT Austin and Kyle Kras, William Walker, and Tiffany Wilson at The Citadel for assistance with sample collection.

Funding

This work was supported by National Science Foundation grants AGS-2503966 to J. W. P., Y. M. O., and D. L., AGS–2103092 to J. W. P. and Y. M. O., OCE-1805874 to J. W. P., F. W. T., and P. N. D., OCE–2043447 and AGS–2103007 to P. N. D., and OCE-0402349 to F. W. T. This work was partially supported by National Taiwan University Core Consortiums Project grants 110L8907 and 113L891902, Higher Education Sprout Project of the Taiwan Ministry of Education grant 112L894202, and the projects under the Taiwan National Science and Technology Council grant 111-2116-M-002-022-MY3 to C.-C. S.

Author contributions

This work was conceptualized by R. A. D., J. W. P., Y. M. O., and F. W. T. The original manuscript and figures were drafted by R. A. D. All authors contributed to the investigation, methodology, and review. Field work was conducted by R. A. D., J. W. P., K. T., F. W. T., A. K., and K. K. K. Computer simulations were executed by P. N. D. and D. L. R. A. D., J. W. P., Y. M. O., K. T., P. N. D., A. E. L., F. W. T., and C.-C. S. contributed to the editing. Funding was acquired by J. W. P., Y. M. O., D. L., F. W. T., P. N. D., and C.-C. S.

Competing interests

The authors declare no competing interests.

Data and materials availability

All instrumental data are publicly available. All previously published model and coral data are available in published repositories, detailed in individual publications (Refs. 20–26, 79–133). New CESM1.2 freshwater forcing simulations are available on request. New coral data are available at https://www.ncei.noaa.gov/access/paleo-search/study/XX (pending). MATLAB code is available through Zenodo at https://doi.org/XX/zenodo.XX (pending).

Supplementary Information Guide

Titles

Supplementary Table 1: Subannually resolved tropical Pacific coral records

Supplementary Table 2: U-series dating report for novel Vanuatu corals.

Supplementary Table 3: Observational products in this study.

Supplementary Table 4: Vanuatu and Kiritimati coral data in this study.

Supplementary Table 5: Background conditions and durations in CESM1.2 simulations.

Supplementary Table 6: Reference intervals and thresholds for extreme El Niño frequencies.

Supplementary Table 1 (.csv file)

This table lists subannually-resolved tropical Pacific coral records, including locations, sample identifiers, ages, record lengths, and references to the original studies. It underpins Fig. 1b and Extended Data Fig. 1b and ensures transparency and reproducibility by documenting the datasets used and provides a consolidated reference for coral records in the tropical Pacific.

Supplementary Tables 2–6 (.pdf file)

These tables present U-series dating results for novel Vanuatu corals, a reference of new and published coral records analysed in this study, observational products, and supporting data sets. Collectively, they document the geochemical and observational foundations of the work and support reproducibility of the analyses.

DOMEYKO_2026 - Supplementary Table 1

Record #	Location	Lat, Lon	Sample name(s)	Genus species	Age (ka BP)	Length (yrs)	References
1	Kiritimati, Kiribati	2°N, 157°W	X16_comp	Porites sp.	-0.062	10	81
2	Sarawak, Malaysia	4°N, 114°E	AG	Porites sp.	-0.061	10	82
3	Lingyang Reef, Yongle Atoll	16°N, 112°E	LY1	Porites sp.	-0.054	19	83
4	Tahiti Is., French Polynesia	18°S, 149°W	TIAREI-4	Porites sp.	-0.054	7	84
5	Tahiti Is., French Polynesia	18°S, 149°W	TIAREI-A1	Porites sp.	-0.054	8	84
6	Tahiti Is., French Polynesia	18°S, 149°W	TIAREI-3B	Porites sp.	-0.054	8	84
7	Tahiti Is., French Polynesia	18°S, 150°W	MARAA-7	Porites sp.	-0.054	8	84
8	Tahiti Is., French Polynesia	18°S, 150°W	MARAA-8	Porites sp.	-0.054	3	84
9	Davies Reef, Australia	19°S, 148°E	DAV09_2 (DAV-1)	Porites lutea	-0.053	13	85
10	Lingyang Reef, Yongle Atoll	16°N, 112°E	LY2	Porites sp.	-0.051	26	83
11	Kosrae Island, Fed. States of Micronesia	5°N, 163°E	KOS	Porites sp.	-0.050	25	86
12	Nomad Reef, Australia	12°S, 143°E	NOM	Porites sp.	-0.050	18	87
13	Clerke Reef, Australia	12°S, 143°E	CLK	Porites sp.	-0.049	12	87
14	Kiritimati, Kiribati	2°N, 157°W	X12-X14_comp	Porites sp.	-0.049	26	23
15	Ngeralang, Palau	8°N, 135°E	NL9	Porites lutea	-0.049	18	88
16	Sarawak, Malaysia	4°N, 114°E	AG	Porites sp.	-0.049	34	82
17	Wolei Atoll, Fed. States of Micronesia	7°N, 144°E	WOL	Porites sp.	-0.049	27	86
18	Bayes Islet, New Caledonia	21°S, 165°E	BayesM	Porites sp.	-0.046	12	89
19	Hon Tre Island, Vietnam	12°N, 109°E	BB	Porites lutea	-0.044	34	90
20	Kiritimati, Kiribati	2°N, 157°W	XM22	Porites sp.	-0.043	29	91
21	Shark Bay, Wolf Island, Ecuador	1°N, 92°W	GW10-10	Porites lobata	-0.043	34	92
22	Palmyra Is., U.S. Territory	6°N, 162°W	PM5	Porites sp.	-0.042	12	93
23	Hon Tre Island, Vietnam	12°N, 109°E	TN	Porites lutea	-0.041	28	90
24	Palmyra Is., U.S. Territory	6°N, 162°W	PM1	Porites sp.	-0.041	14	93
25	Tabuaeran, Kiribati	4°N, 159°W	---	Porites sp.	-0.039	33	94
26	Huon Peninsula, Papua New Guinea	6°S, 148°E	H95-64	Porites sp.	-0.037	19	95
27	Ngaragabel, Palau	7°N, 134°E	NGB	Porites lutea	-0.036	45	88
28	Butaritari Atoll, Kiribati	3°N, 173°E	BUT 3-2	Porites sp.	-0.035	51	96
29	Eel Reef, Australia	13°S, 144°E	EEL	Porites sp.	-0.035	11	87
30	Kiritimati, Kiribati	2°N, 157°W	---	Porites sp.	-0.035	26	94
31	Great Keppel Island, Australia	23°S, 151°E	GK2	Porites sp.	-0.034	53	97
32	Portland Roads, Australia	13°S, 143°E	POR	Porites sp.	-0.034	13	87
33	Clipperton Island	10°N, 109°W	3C	Porites lobata	-0.032	25	98
34	Reef 13-050, Australia	13°S, 144°E	13-050	Porites sp.	-0.032	16	87
35	Malo Channel, Vanuatu	16°S, 167°E	KIL04 18O	Porites sp.	-0.031	23	99
36	Tabuaeran, Kiribati	4°N, 159°W	fann_mod_spl	Porites sp.	-0.028	57	22
37	Shark Bay, Wolf Island, Ecuador	1°N, 92°W	GW10-3	Porites lobata	-0.025	70	92
38	Kiritimati, Kiribati	2°N, 158°W	Kiritimati_mod	Porites sp.	-0.023	70	25
39	Savusavu Bay, Vanua Levu, Fiji	17°S, 179°E	LH	Diploastrea heliopora	-0.021	62	100
40	Doangdoangan Besar, Indonesia	5°S, 118°E	DD1	Porites sp.	-0.019	84	101
41	Savusavu Bay, Vanua Levu, Fiji	17°S, 179°E	4F1	Diploastrea heliopora	-0.019	57	100
42	Kiritimati, Kiribati	2°N, 157°W	PP7-3	Porites sp.	-0.016	55	80
43	Espiritu Santo Is., Vanuatu	16°S, 167°E	MCB	Porites lutea	-0.011	64	99
44	Punta Pitt, Isla San Cristobal, Ecuador	1°S, 89°W	---	Pavona clavus	-0.009	47	102
45	Madang Lagoon, Papua New Guinea	5°S, 146°E	Madang-1a	Porites sp.	-0.007	69	103
46	Muschu Is., Papua New Guinea	3°S, 144°E	MS01	Porites sp.	-0.004	88	104
47	Rock Islands, Palau	7°N, 134°E	RI6	Porites lutea	-0.004	109	105
48	Rarotonga, Cook Islands	21°S, 160°W	99	Porites lutea	-0.003	93	106

49	Nauru Island, Republic of Nauru	1°S, 167°E	Nauru-2	Porites sp.	0.004	98	107
50	Palaui Island, Philippines	19°N, 122°E	PL1	Porites lobata	0.004	132	108
51	Palmyra Is., U.S. Territory	6°N, 162°W	Palmyra_mod	Porites sp.	0.006	112	109
52	Nauru Island, Republic of Nauru	1°S, 167°E	Nauru-1	Porites australiensis	0.007	104	107
53	Palmyra Is., U.S. Territory	6°N, 162°W	PM	Porites lutea	0.008	112	110
54	Tarawa, Kiribati	1°N, 173°E	TARO	Porites sp.	0.008	96	111
55	Laing, Papua New Guinea	4°S, 145°E	Dur-2	Porites sp.	0.011	110	95
56	Madang, Papua New Guinea	5°S, 146°E	DT91-7	Porites sp.	0.013	113	95
57	Rarotonga, Cook Islands	21°S, 160°W	3R	Porites lutea	0.013	126	106
58	Clipperton Island	10°N, 109°W	C2B, C4B, C6A, CF1B	Porites lobata	0.016	120	112
59	Rabaul, East New Britain, Papua New Guinea	4°S, 152°E	98RK-3	Porites lobata	0.018	130	113
60	Misima Island, Papua New Guinea	11°S, 153°E	MiC	Porites sp.	0.019	28	114
61	Kiritimati, Kiribati	2°N, 157°W	X13-X14_comp	Porites sp.	0.020	15	79
62	Tabuaeran, Kiribati	4°N, 159°W	F4	Porites sp.	0.024	37	115
63	Bunaken Island, Indonesia	2°N, 125°E	Bunaken	Porites sp.	0.025	131	116
64	Sabine Bank, Vanuatu	16°S, 166°E	06-SB-A	Porites sp.	0.025	164	24,117
65	Moorea, French Polynesia	18°S, 150°W	---	Porites lutea	0.029	137	118
66	Maiana, Kiribati	1°N, 173°E	MAI95-2-3	Porites sp.	0.033	155	119
67	Clarion Island, Mexico	18°N, 115°W	---	Porites sp.	0.041	179	120
68	Houbihu, Taiwan	22°N, 121°E	HBH	Porites sp.	0.049	225	121
69	Ulong Channel, Palau	7°N, 134°E	UC	Porites lutea	0.049	215	105
70	Double Reef, Guam	14°N, 145°E	GD2	Porites lobata	0.055	210	122
71	Vanua Levu, Fiji	17°S, 179°E	1F	Porites lutea	0.061	216	123
72	Tabuaeran, Kiribati	4°N, 159°W	F5	Porites sp.	0.075	24	115
73	Rarotonga, Cook Islands	21°S, 160°W	2R	Porites lutea	0.088	270	106
74	Secas Island, Panama	8°N, 82°W	S1	Porites lobata	0.104	277	124
75	Amedee Island, New Caledonia	22°S, 166°E	92PAA1, 92PAA2, 99PA	Porites lutea	0.126	351	125
76	Ta'u, American Samoa	14°S, 170°W	Tau-1	Porites sp.	0.184	492	126
77	Palmyra Is., U.S. Territory	6°N, 162°W	SPL17	Porites sp.	0.281	69	127
78	Kiritimati, Kiribati	2°N, 157°W	m2	Porites sp.	0.411	47	22
79	Misima Island, Papua New Guinea	11°S, 153°E	MiG-MiF	Porites sp.	0.422	233	114
80	Palmyra Is., U.S. Territory	6°N, 162°W	SPL14	Porites sp.	0.559	148	127
81	Palmyra Is., U.S. Territory	6°N, 162°W	SB17	Porites sp.	0.765	72	127
82	Espiritu Santo Is., Vanuatu	16°S, 167°E	11-TM-S5	Porites sp.	0.840	100	24
83	Palmyra Is., U.S. Territory	6°N, 162°W	NB12	Porites sp.	1.005	34	127
84	Kiritimati, Kiribati	2°N, 157°W	p49	Porites sp.	1.258	20	22
85	Kiritimati, Kiribati	2°N, 157°W	p2	Porites sp.	1.695	22	22
86	Kiritimati, Kiribati	2°N, 157°W	CW-2	Porites sp.	1.908	23	128
87	Kiritimati, Kiribati	2°N, 157°W	p37	Porites sp.	2.286	27	22
88	Madang, Papua New Guinea	6°S, 148°E	M93TBFC	Porites sp.	2.479	41	95
89	Kiritimati, Kiribati	2°N, 157°W	X12-D2-5	Porites sp.	2.510	17	23
90	Laing, Papua New Guinea	4°S, 145°E	FC2	Porites sp.	2.652	96	95
91	Muschu Is., Papua New Guinea	3°S, 144°E	FM09	Porites sp.	2.660	19	104
92	Kiritimati, Kiribati	2°N, 157°W	XM1	Porites sp.	2.909	21	129
93	Kiritimati, Kiribati	2°N, 157°W	X13-FS21-36	Porites sp.	2.914	10	23
94	Tabuaeran, Kiribati	4°N, 159°W	v10	Porites sp.	3.035	82	22
95	Kiritimati, Kiribati	2°N, 157°W	X12-D1-6	Porites sp.	3.248	13	23
96	Kiritimati, Kiribati	2°N, 157°W	X12-D1-4	Porites sp.	3.414	21	23
97	Kiritimati, Kiribati	2°N, 157°W	p26	Porites sp.	3.454	44	22
98	Kiritimati, Kiribati	2°N, 157°W	XM9	Porites sp.	3.552	35	129
99	Kiritimati, Kiribati	2°N, 157°W	X12-D2-1	Porites sp.	3.765	20	23

100	Kiritimati, Kiribati	2°N, 157°W	p43	Porites sp.	3.819	44	22
101	Kiritimati, Kiribati	2°N, 157°W	p40	Porites sp.	3.951	49	22
102	Bayes Islet, New Caledonia	21°S, 165°E	Bayes1	Porites sp.	3.990	49	89
103	Espiritu Santo Is., Vanuatu	16°S, 167°E	11-TVS-B	Porites sp.	4.028	35	This study
104	Kiritimati, Kiribati	2°N, 157°W	p34	Porites sp.	4.076	70	22
105	Kiritimati, Kiribati	2°N, 157°W	X13-FS21-51	Porites sp.	4.118	14	23
106	Espiritu Santo Is., Vanuatu	16°S, 167°E	---	Porites sp.	4.150	47	130
108	Kiritimati, Kiribati	2°N, 157°W	X13-FS21-14	Porites sp.	4.534	7	23
109	Kiritimati, Kiribati	2°N, 157°W	X13-FS21-38	Porites sp.	4.737	7	23
110	Kiritimati, Kiribati	2°N, 157°W	X13-FS27-2	Porites sp.	4.798	16	23
111	Kiritimati, Kiribati	2°N, 157°W	p382	Porites sp.	4.959	38	22
112	Kiritimati, Kiribati	2°N, 157°W	p381	Porites sp.	5.006	28	22
113	Kiritimati, Kiribati	2°N, 157°W	X13-FS21-15	Porites sp.	5.036	18	23
114	Kiritimati, Kiribati	2°N, 157°W	X13-FS21-40	Porites sp.	5.049	10	23
115	Kiritimati, Kiribati	2°N, 157°W	p11	Porites sp.	5.068	23	22
116	Kiritimati, Kiribati	2°N, 157°W	X13-FS21-22	Porites sp.	5.103	8	23
117	Kiritimati, Kiribati	2°N, 157°W	X13-FS21-45a	Porites sp.	5.136	8	23
118	Kiritimati, Kiribati	2°N, 157°W	X13-FS21-45b	Porites sp.	5.141	5	23
119	Kiritimati, Kiribati	2°N, 157°W	X13-FS21-16	Porites sp.	5.224	17	23
120	Muschu Is., Papua New Guinea	3°S, 144°E	FM22	Porites sp.	5.433	25	104
121	Muschu Is., Papua New Guinea	3°S, 144°E	FM21	Porites sp.	5.843	24	104
122	Muschu Is., Papua New Guinea	3°S, 144°E	FM07	Porites sp.	5.860	9	104
123	Tabuaeran, Kiribati	4°N, 159°W	v30	Porites sp.	5.979	42	22
124	Tabuaeran, Kiribati	4°N, 159°W	v13	Porites sp.	6.020	27	22
125	Muschu Is., Papua New Guinea	3°S, 144°E	FM15	Porites sp.	6.070	89	104
126	Tabuaeran, Kiribati	4°N, 159°W	v8	Porites sp.	6.077	42	22
127	Kiritimati, Kiribati	2°N, 157°W	X13-FS22-8	Porites sp.	6.322	24	23
128	Tabuaeran, Kiribati	4°N, 159°W	v28	Porites sp.	6.350	21	22
129	Huon Peninsula, Papua New Guinea	6°S, 148°E	H95-16	Porites sp.	6.475	50	95
130	Tabuaeran, Kiribati	4°N, 159°W	v33	Porites sp.	6.593	25	22
131	Ratua Island, Vanuatu	16°S, 167°E	Psp-06-09	Porites sp.	6.650	25	131
132	Tabuaeran, Kiribati	4°N, 159°W	v11	Porites sp.	6.878	38	22
133	Muschu Is., Papua New Guinea	3°S, 144°E	FM23	Porites sp.	7.040	18	104
134	Araki Is., Vanuatu	16°S, 167°E	05-AR-I	Porites sp.	7.172	42	This study
135	Muschu Is., Papua New Guinea	3°S, 144°E	FM24	Porites sp.	7.225	18	104
136	Koil Is., Papua New Guinea	3°S, 144°E	FK05	Porites sp.	7.567	33	104
137	Tahiti Is., French Polynesia	18°S, 150°W	310-7A-13R-1	Porites sp.	9.060	5	84
138	Tahiti Is., French Polynesia	18°S, 150°W	310-7A-15R-1	Porites sp.	9.370	4	84
139	Tahiti Is., French Polynesia	18°S, 150°W	310-7A-18R-1	Porites sp.	10.030	6	84
140	Tahiti Is., French Polynesia	18°S, 150°W	310-5A-12R-1	Porites sp.	11.030	15	84
141	Espiritu Santo Is., Vanuatu	16°S, 167°E	19-TV-J	Porites sp.	11.991	59	This study
142	Espiritu Santo Is., Vanuatu	16°S, 167°E	---	Diploastrea heliopora	12.107	35	26
143	Tahiti Is., French Polynesia	17°S, 149°W	310-23A-5R-1	Porites sp.	12.330	1	84
144	Espiritu Santo Is., Vanuatu	16°S, 167°E	19-TV-K	Porites sp.	12.337	38	This study
145	Tahiti Is., French Polynesia	17°S, 149°W	310-23A-6R-1	Porites sp.	12.404	10	132
146	Tahiti Is., French Polynesia	18°S, 150°W	310-18A-18R-1	Porites sp.	14.100	8	84
147	Tahiti Is., French Polynesia	18°S, 150°W	310-18A-19R-1	Porites sp.	14.140	10	84
148	Tahiti Is., French Polynesia	17°S, 149°W	310-9D-7R-1	Porites sp.	14.221	16	132
149	Tahiti Is., French Polynesia	17°S, 149°W	310-9A-6R-1	Porites sp.	14.250	3	84
150	Tahiti Is., French Polynesia	18°S, 150°W	310-20A-23R-1	Porites sp.	14.350	5	84
151	Tahiti Is., French Polynesia	17°S, 149°W	310-9E-9R-1	Porites sp.	14.360	2	84

152	Tahiti Is., French Polynesia	18°S, 150°W	310-20A-22R-2	Porites sp.	14.370	7	84
153	Tahiti Is., French Polynesia	18°S, 150°W	310-20A-23R-1	Porites sp.	14.460	33	84
154	Tahiti Is., French Polynesia	17°S, 149°W	310-9D-9R-1	Porites sp.	14.660	4	84
155	Tahiti Is., French Polynesia	18°S, 150°W	310-18A-22R-1	Porites sp.	14.740	3	84
156	Tahiti Is., French Polynesia	18°S, 150°W	310-20A-24R-1	Porites sp.	14.740	7	84
157	Espiritu Santo Is., Vanuatu	16°S, 167°E	19-TV-2	Porites sp.	14.955	64	This study
158	Tahiti Is., French Polynesia	17°S, 149°W	310-24A-11R-2	Porites sp.	14.994	22	133
159	Tahiti Is., French Polynesia	17°S, 149°W	310-24A-13R-1	Porites sp.	15.150	9	84

Supplementary Table 2: U-series dating report for novel Vanuatu corals.

Sample* ID	^{238}U 10^{-9} g/g[a]	^{232}Th 10^{-12} g/g	$\delta^{234}U$ measured[a]	[$^{230}Th/^{238}U$] activity[c]	$^{230}Th/^{232}Th$ atomic (x 10^{-3})	Age (kyr ago) uncorrected	Age (ka) corrected[c,d]	$\delta^{234}U_{initial}$ corrected[b]
11-TVS-B	2530.3 ± 2.7	1538.3 ± 7.6	143.0 ± 1.8	0.04218 ± 0.00011	1.1457 ± 0.0063	4.103 ± 0.013	4.028 ± 0.015	144.7 ± 1.8
05-AR-I	2627.7 ± 4.7	17 ± 24	144.6 ± 2.3	0.07341 ± 0.00041	190 ± 270	7.229 ± 0.044	7.172 ± 0.044	147.6 ± 2.4
19-TV-J	2358.4 ± 2.4	153.1 ± 2.1	140.7 ± 1.4	0.11970 ± 0.00022	30.41 ± 0.43	12.062 ± 0.028	11.991 ± 0.028	145.6 ± 1.5
19-TV-K	2320.0 ± 2.3	10.2 ± 2.2	138.1 ± 1.5	0.12266 ± 0.00040	460 ± 100	12.407 ± 0.047	12.337 ± 0.047	143.0 ± 1.6
19-TV-2	2618.7 ± 2.6	847.9 ± 2.6	134.9 ± 1.2	0.14652 ± 0.00025	7.461 ± 0.025	15.032 ± 0.033	14.955 ± 0.033	140.8 ± 1.3

*Chemistry was performed in October 2011 for 11-TVS-B, January 2007 for 05-AR-I, October 2019 for 19-TV-2, and January 2020 for 19-TV-J and -K.

Analytical errors are 2σ of the mean.

$\delta^{234}U = ([^{234}U/^{238}U]_{activity} - 1) \times 1000$.

[a] $[^{238}U] = [^{235}U] \times 137.77$ (±0.11‰) (Ref 134); $\delta^{234}U = ([^{234}U/^{238}U]_{activity} - 1) \times 1000$.

[b] $\delta^{234}U_{initial}$ corrected was calculated based on ^{230}Th age (T), i.e., $\delta^{234}U_{initial} = \delta^{234}U_{measured} \times e^{\lambda_{234} \times T}$, and T is corrected age.

[c] $[^{230}Th/^{238}U]_{activity} = 1 - e^{-\lambda_{230}T} + (\delta^{234}U_{measured}/1000)[\lambda_{230}/(\lambda_{230} - \lambda_{234})](1 - e^{-(\lambda_{230} - \lambda_{234})T})$, where T is the age.

Decay constants used for age calculation are 2.8215×10^{-6} yr^{-1} for ^{234}U from Hu et al. (2025; Ref 52) and others available in Cheng et al. (2013; Ref 53).

[d] Age corrections, relative to 1950 AD, were calculated using an estimated atomic $^{230}Th/^{232}Th$ ratio of 4 (± 2) x 10^{-6} (Ref 135)..

Supplementary Table 3: Observational products in this study.

Product	Resolution	Variable(s)	Years (CE)	Length (years)	References
COBE	1° x 1°	SST	1850–2025	176	61
ERSSTv5	2° x 2°	SST	1854–2025	172	56
HadCRUT4.6G	5° x 5°	SSTA	1850–2017	168	63
HadCRUT5	5° x 5°	SSTA	1850–2025	176	64
HadCRUT5inf	5° x 5°	SSTA	1850–2025	176	64
HadISST	1° x 1°	SST	1870–2025	156	65
KaplanSSTv2	5° x 5°	SSTA	1856–2022	167	66
ORA-20C (reanalysis)	1° x 1°	SST, SSS	1900–2009	110	54
SODA (reanalysis)	0.5° x 0.5°	SST, SSS	1871–2010	140	55
Delcroix	1° x 1°	SSS	1950–2009	60	57

HadCRUT, HadSST, and KaplanSST products are available as monthly anomalies from the global mean. Local monthly anomalies were computed using a 1961–1990 CE climatological reference period. The ORA-20C, SODA, and Delcroix products were used to compute the forward-modelled $\delta^{18}O$ annual cycle at Kiritimati (see Extended Data Fig. 9b).

Supplementary Table 4: Vanuatu and Kiritimati coral data in this study.

Location	Sample name	Age (ka BP)	Length (yrs)	References
Sabine Bank, Vanuatu	06-SB-A	-0.025†	164	24,117
Tasmaloum, Vanuatu	11-TM-S	0.848†	100	24
Tavovusvus, Vanuatu	11-TVS-B	4.028	43	**This study**
Araki, Vanuatu	05-AR-I	7.172	42	**This study**
Tavovusvus, Vanuatu	19-TV-J	11.991	59	**This study**
Tavovusvus, Vanuatu	19-TV-K	12.337	38	**This study**
Tavovusvus, Vanuatu	19-TV-2	14.955	64	**This study**
Kiritimati, Kiribati	Mult. records*	-0.062	10	81
Kiritimati, Kiribati	Mult. records**	-0.049	26	23
Kiritimati, Kiribati	PP7-3	0.016	55	80
Kiritimati, Kiribati	Mult. records***	0.020	15	79
Kiritimati, Kiribati	Compilation	-0.020††	93	**This study**
Kiritimati, Kiribati	M2	0.457††	45	22
Kiritimati, Kiribati	P49	1.277††	18	22
Kiritimati, Kiribati	P2	1.716	20	22
Kiritimati, Kiribati	P37	2.311	25	22
Kiritimati, Kiribati	X12-D2-5	2.510	17	23
Kiritimati, Kiribati	X13-FS21-36	2.914	10	23
Kiritimati, Kiribati	XM1	2.928	18	129
Kiritimati, Kiribati	X12-D1-6	3.248	13	23
Kiritimati, Kiribati	X12-D1-4	3.414	21	23
Kiritimati, Kiribati	P26	3.498	43	22
Kiritimati, Kiribati	XM9	3.585	32	129
Kiritimati, Kiribati	X12-D2-1	3.765	20	23
Kiritimati, Kiribati	P43	3.862	43	22
Kiritimati, Kiribati	P40	3.998	47	22
Kiritimati, Kiribati	X13-FS21-51	4.118	14	23
Kiritimati, Kiribati	P34	4.144	67	22
Kiritimati, Kiribati	XM35	4.419	176	25
Kiritimati, Kiribati	X13-FS21-14	4.534	7	23
Kiritimati, Kiribati	X13-FS21-38	4.737	7	23
Kiritimati, Kiribati	X13-FS27-2	4.798	16	23
Kiritimati, Kiribati	P382	4.996	36	22
Kiritimati, Kiribati	P381	5.033	26	22
Kiritimati, Kiribati	X13-FS21-15	5.036	18	23
Kiritimati, Kiribati	X13-FS21-40	5.049	10	23
Kiritimati, Kiribati	P11	5.108	22	22
Kiritimati, Kiribati	X13-FS21-22	5.103	8	23
Kiritimati, Kiribati	X13-FS21-45a	5.136	8	23
Kiritimati, Kiribati	X13-FS21-45b	5.141	5	23
Kiritimati, Kiribati	X13-FS21-16	5.224	17	23
Kiritimati, Kiribati	X13-FS22-8	6.322	24	23

*Multiple records: X16C-D3, X16C-D4, X16C-D5, X16C-D10, X16A-D1, and X16A-D2, spliced and averaged as published.

**Multiple records: X12-6, X12-3, X14-1, X14-14, X14-7, and X14-9, spliced and averaged as published.

***Multiple records: X13-FS17-8 and X14-FS28-10, spliced with the annual cycle of PP7-3 (Ref 80) in the January 1929 CE to February 1930 CE interval.

GPS coordinates for coral collection sites are in Supplementary Table 1. Compilation at Kiritimati combines and replaces the four published records above it (Methods). Grey shading denotes coral records included in the extreme-event frequency analysis in Fig. 4. The † symbol denotes coral records included in the 1.5–0-ka reference interval for Vanuatu in Fig. 4b. The †† symbol denotes coral records included in the 1.5–0-ka reference interval for Kiritimati in Fig. 4c.

Supplementary Table 5: Background conditions and durations in CESM1.2 simulations.

Simulation	Duration (years)	Relative sea level (m)	CO_2 (ppm)	CH_4 (ppm)	N_2O (ppb)	Freshwater forcing (Sv)
2xCO2	400	0	560	760	270	0
PI control	1500	0	280	760	270	0
3 ka	500	0	275	580	270	0
6 ka	500	0	265	600	260	0
9 ka	500	-20	260	665	260	0
12 ka	500	-60	250	475	245	0
12-ka FWF	500	-60	250	475	245	0.2
15 ka	500	-100	230	475	240	0
15-ka FWF	500	-100	230	475	240	0.2

Ice sheet topography and land surface glacier extent were prescribed based on the ICE-6G_C reconstruction[136, 137]. Changes in vegetation are documented in Thirumalai et al.[21] (2024). Freshwater forcing (FWF) simulations were imposed at the ocean surface of the gridded quadrant at 50–70°N, 80°W–20°E.

Supplementary Table 6: Reference intervals and thresholds for extreme El Niño frequencies.

Source data	Site	Reference interval	Variable	Percentile	NDJ threshold (units)
CESM1.2	Niño 3.4	PI control	SST	93rd	2.50 (°C)
Coral	Vanuatu	1.5-0 ka	$\delta^{18}O$	93rd	0.19 (‰)
CESM1.2	SWP	PI control	$\delta^{18}O_{PSM}$	93rd	0.23 (‰)
Coral	Kiritimati	1.5-0 ka	$\delta^{18}O$	7th	-0.19 (‰)
CESM1.2	CEP	PI control	$\delta^{18}O_{PSM}$	7th	-0.37 (‰)

The southwest Pacific (SWP; 14.5–16.5°S, 162.5–165.5°E) in CESM1.2 is the area most representative of modern Vanuatu climate conditions (Methods). The central equatorial Pacific (CEP; 2°N, 157.5°W) in CESM1.2 is the model representation for Kiritimati. Extreme El Niño frequency is the number of events century^{-1} where the NDJ average of anomalies exceeds the threshold tailward, i.e., above the 93rd percentile threshold for Niño 3.4 and Vanuatu/SWP and below the 7th percentile threshold for Kiritimati/CEP.

Supplementary references

82. Krawczyk, H. *et al.* Corals reveal ENSO-driven synchrony of climate impacts on both terrestrial and marine ecosystems in northern Borneo. *Scientific Reports* **10**, 3678 (2020).

83. Chen, T. *et al.* Coral-Derived Western Pacific Tropical Sea Surface Temperatures During the Last Millennium. *Geophysical Research Letters* **45**, 3542–3549 (2018).

84. Knebel, O. *et al.* Last Deglacial Environmental Change in the Tropical South Pacific From Tahiti Corals. *Paleoceanography and Paleoclimatology* **39**, 0 (2024).

85. D'Olivo, J. P., Sinclair, D. J., Rankenburg, K. & McCulloch, M. T. A universal multi-trace element calibration for reconstructing sea surface temperatures from long-lived Porites corals: Removing 'vital-effects'. *Geochimica et Cosmochimica Acta* **239**, 109–135 (2018).

86. Mohtar, A. T. *et al.* Coral-based proxy calibrations constrain ENSO-driven sea surface temperature and salinity gradients in the Western Pacific Warm Pool. *Palaeogeography, Palaeoclimatology, Palaeoecology* **561**, 110037 (2021).

87. Reed, E. V., Cole, J. E., Lough, J. M., Thompson, D. & Cantin, N. E. Linking climate variability and growth in coral skeletal records from the Great Barrier Reef. *Coral Reefs* **38**, 29–43 (2019).

88. Osborne, M. C., Dunbar, R. B., Mucciarone, D. A., Sanchez-Cabeza, J.-A. & Druffel, E. Regional calibration of coral-based climate reconstructions from Palau, West Pacific Warm Pool (WPWP). *Palaeogeography, Palaeoclimatology, Palaeoecology* **386**, 308–320 (2013).

89. Emile-Geay, J. *et al.* Links between tropical Pacific seasonal, interannual and orbital variability during the Holocene. *Nature Geoscience* **9**, 168–173 (2016).

90. Bolton, A. *et al.* Paired Porites coral Sr/Ca and δ18O from the western South China Sea: Proxy calibration of sea surface temperature and precipitation. *Palaeogeography …* (2014).

91. McGregor, H. V., Fischer, M. J., Gagan, M. K., Fink, D. & Woodroffe, C. D. Environmental control of the oxygen isotope composition of Porites coral microatolls. *Geochimica et Cosmochimica Acta* **75**, 3930–3944 (2011).

92. Jimenez, G., Cole, J. E., Thompson, D. M. & Tudhope, A. W. Northern Galápagos Corals Reveal Twentieth Century Warming in the Eastern Tropical Pacific. *Geophysical Research Letters* **45**, 1981–1988 (2018).

93. Sayani, H. R., Cobb, K. M., DeLong, K., Hitt, N. T. & Druffel, E. R. M. Intercolony δ18O and Sr/Ca variability among Porites spp. corals at Palmyra Atoll: Toward more robust coral-based estimates of climate. *Geochemistry, Geophysics, Geosystems* **20**, 5270–5284 (2019).

94. Nurhati, I. S., Cobb, K. M., Charles, C. D. & Dunbar, R. B. Late 20th century warming and freshening in the central tropical Pacific. *Geophysical Research Letters* **36**, 66 (2009).

95. Tudhope, A. W. *et al.* Variability in the El Niño-Southern Oscillation through a glacial-interglacial cycle. *Science* **291**, 1511–1517 (2001).

96. Carilli, J. E. *et al.* Equatorial Pacific coral geochemical records show recent weakening of the Walker Circulation. *Paleoceanography* **29**, 1031–1045 (2014).

97. Saha, N. *et al.* Seasonal to decadal scale influence of environmental drivers on Ba/Ca and Y/Ca in coral aragonite from the southern Great Barrier Reef. *Science of the Total Environment* **639**, 1099–1109 (2018).

98. Linsley, B. K., Messier, R. G. & Dunbar, R. B. Assessing between-colony oxygen isotope variability in the coral Porites lobata at Clipperton Atoll. *Coral Reefs* (1999).

99. Kilbourne, K. H., Quinn, T. M., Taylor, F. W., Delcroix, T. & Gouriou, Y. El Niño-Southern Oscillation-related salinity variations recorded in the skeletal geochemistry of a Porites coral from Espiritu Santo, Vanuatu. *Paleoceanography* **19**, PA4002 (2004).

100. Bagnato, S., Linsley, B. K., Howe, S. S., Wellington, G. M. & Salinger, J. Evaluating the use of the massive coral Diploastrea heliopora for paleoclimate reconstruction. *Paleoceanography* **19**, (2004).

101. Murty, S. A. *et al.* Climatic Influences on Southern Makassar Strait Salinity Over the Past Century. *Geophysical Research Letters* **44**, 19 (2017).

102. Shen, G. T. *et al.* Surface ocean variability at Galapagos from 1936–1982: Calibration of geochemical tracers in corals. *Paleoceanography* **7**, 563–588 (1992).

103. Tudhope, A. W. *et al.* Recent changes in climate in the far western equatorial Pacific and their relationship to the Southern Oscillation; oxygen isotope records from massive corals, Papua New Guinea. *Earth and Planetary Science Letters* **136**, 575–590 (1995).

104. McGregor, H. V. & Gagan, M. K. Diagenesis and geochemistry of Porites corals from Papua New Guinea: Implications for paleoclimate reconstruction. *Geochimica et Cosmochimica Acta* **67**, 2147–2156 (2003).

105. Osborne, M. C., Dunbar, R. B., Mucciarone, D. A., Druffel, E. & Sanchez-Cabeza, J.-A. A 215-yr coral δ18O time series from Palau records dynamics of the West Pacific Warm Pool following the end of the Little Ice Age. *Coral Reefs* **33**, 719–731 (2014).

106. Linsley, B. K. *et al.* Tracking the extent of the South Pacific Convergence Zone since the early 1600s. *Geochemistry, Geophysics, Geosystems* **7**, 118 (2006).

107. Guilderson, T. P. & Schrag, D. P. Reliability of coral isotope records from the western Pacific warm pool: A comparison using age-optimized records. *Paleoceanography* **14**, 457–464 (1999).

108. Ramos, R. D., Goodkin, N. F., Siringan, F. P. & Hughen, K. A. Coral Records of Temperature and Salinity in the Tropical Western Pacific Reveal Influence of the Pacific Decadal Oscillation Since the Late Nineteenth Century. *Paleoceanography and Paleoclimatology* **34**, 1344–1358 (2019).

109. Cobb, K. M., Charles, C. D. & Hunter, D. E. A central tropical Pacific coral demonstrates Pacific, Indian, and Atlantic decadal climate connections. *Geophysical Research Letters* **28**, 2209–2212 (2001).

110. Nurhati, I. S., Cobb, K. M. & Di Lorenzo, E. Decadal-Scale SST and Salinity Variations in the Central Tropical Pacific: Signatures of Natural and Anthropogenic Climate Change. *Journal of Climate* **24**, 3294–3308 (2011).

111. Cole, J. E., Fairbanks, R. G. & Shen, G. T. Recent Variability in the Southern Oscillation: Isotopic Results from a Tarawa Atoll Coral. *Science* **260**, 1790–1793 (1993).

112. Wu, H. C., Moreau, M., Linsley, B. K., Schrag, D. P. & Corrège, T. Investigation of sea surface temperature changes from replicated coral Sr/Ca variations in the eastern equatorial Pacific (Clipperton Atoll) since 1874. *Palaeogeography, Palaeoclimatology, Palaeoecology* **412**, 208–222 (2014).

113. Quinn, T. M., Taylor, F. W. & Crowley, T. J. Coral-based climate variability in the Western Pacific Warm Pool since 1867. *Journal of Geophysical Research* **111**, (2006).

114. Hereid, K. A. *et al.* Coral record of reduced El Nino activity in the early 15th to middle 17th centuries. *Geology* **41**, 51–54 (2013).

115. Sanchez, S. C. *et al.* A Continuous Record of Central Tropical Pacific Climate Since the Midnineteenth Century Reconstructed From Fanning and Palmyra Island Corals: A Case Study in Coral Data Reanalysis. *Paleoceanography and Paleoclimatology* **35**, 19 (2020).

116. Charles, C. D., Cobb, K., Moore, M. D. & Fairbanks, R. G. Monsoon–tropical ocean interaction in a network of coral records spanning the 20th century. *Marine Geology* **201**, 207–222 (2003).

117. Gorman, M. K. *et al.* A coral-based reconstruction of sea surface salinity at Sabine Bank, Vanuatu from 1842 to 2007 CE. *Paleoceanography* **27**, PA3226 (2012).

118. Boiseau, M., Ghil, M. & Juillet-Leclerc, A. Climatic trends and interdecadal variability from south-central Pacific coral records. *Geophysical Research Letters* **26**, 2881–2884 (1999).

119. Urban, F. E., Cole, J. E. & Overpeck, J. T. Influence of mean climate change on climate variability from a 155-year tropical Pacific coral record. *Nature* **407**, 989–993 (2000).

120. Sanchez, S. C., Charles, C. D., Carriquiry, J. D. & Villaescusa, J. A. Two centuries of coherent decadal climate variability across the Pacific North American region. *Geophysical Research Letters* **43**, 9208–9216 (2016).

121. Ramos, R. D., Goodkin, N. F. & Fan, T. Coral Records at the Northern Edge of the Western Pacific Warm Pool Reveal Multiple Drivers of Sea Surface Temperature, Salinity, and Rainfall Variability Since the End of the Little Ice Age. *Paleoceanography and Paleoclimatology* **35**, 21 (2020).

122. Asami, R. *et al.* Interannual and decadal variability of the western Pacific sea surface condition for the years 1787–2000: Reconstruction based on stable isotope record from a Guam coral. *Journal of Geophysical Research: Oceans* **110**, 73 (2005).

123. Linsley, B. K. *et al.* Geochemical evidence from corals for changes in the amplitude and spatial pattern of South Pacific interdecadal climate variability over the last 300 years. *Climate Dynamics* **22**, 1–11 (2004).

124. Linsley, B. K., Dunbar, R. B., Wellington, G. M. & Mucciarone, D. A. A coral-based reconstruction of Intertropical Convergence Zone variability over Central America since 1707. *Journal of Geophysical Research: Oceans* **99**, 9977–9994 (1994).

125. DeLong, K. L., Quinn, T. M., Taylor, F. W., Shen, C.-C. & Lin, K. Improving coral-base paleoclimate reconstructions by replicating 350years of coral Sr/Ca variations. *Palaeogeography, Palaeoclimatology, Palaeoecology* **373**, 6–24 (2013).

126. Tangri, N., Dunbar, R. B., Linsley, B. K. & Mucciarone, D. M. ENSO's Shrinking Twentieth-Century Footprint Revealed in a Half-Millennium Coral Core From the South Pacific Convergence Zone. *Paleoceanography and Paleoclimatology* **33**, 1136–1150 (2018).

127. Cobb, K. M., Charles, C. D., Cheng, H. & Edwards, R. L. El Niño/Southern Oscillation and tropical Pacific climate during the last millennium. *Nature* **424**, 271–276 (2003).

128. Woodroffe, C. D. & Gagan, M. K. Coral microatolls from the central Pacific record Late Holocene El Niño. *Geophysical Research Letters* **27**, 1511–1514 (2000).

129. Woodroffe, C. D., Beech, M. R. & Gagan, M. K. Mid-late Holocene El Niño variability in the equatorial Pacific from coral microatolls. *Geophysical Research Letters* **30**, 1358 (2003).

130. Corrège, T. *et al.* Evidence for stronger El Niño-Southern Oscillation (ENSO) events in a mid-Holocene massive coral. *Paleoceanography* **15**, 465–470 (2000).

131. Duprey, N. *et al.* Early mid-Holocene SST variability and surface-ocean water balance in the southwest Pacific. *Paleoceanography* **27**, 34 (2012).

132. Asami, R. *et al.* Evidence for tropical South Pacific climate change during the Younger Dryas and the Bølling–Allerød from geochemical records of fossil Tahiti corals. *Earth and Planetary Science Letters* **288**, 96–107 (2009).

133. Felis, T. *et al.* Pronounced interannual variability in tropical South Pacific temperatures during Heinrich Stadial 1. *Nature Communications* **3**, 965 (2012).

134. Hiess, J., Condon, D. J., McLean, N. & Noble, S. R. 238U/235U systematics in terrestrial uranium-bearing minerals. *Science* **335**, 1610–1614 (2012).

135. Shen, C.-C. *et al.* Variation of initial 230Th/232Th and limits of high precision U–Th dating of shallow-water corals. *Geochimica et Cosmochimica Acta* **72**, 4201–4223 (2008).

136. Argus, D. F., Peltier, W. R., Drummond, R. & Moore, A. W. The Antarctica component of postglacial rebound model ICE-6G_C (VM5a) based on GPS positioning, exposure age

dating of ice thicknesses, and relative sea level histories. *Geophysical Journal International* **198**, 537–563 (2014).

137. Peltier, W. R., Argus, D. F. & Drummond, R. Space geodesy constrains ice age terminal deglaciation: The global ICE-6G_C (VM5a) model. *Journal of Geophysical Research: Solid Earth* **120**, 450–487 (2015).